Materials Today Bio 40 (2026) 103539

Contents lists available at ScienceDirect

Materials Today Bio

journal homepage: www.journals.elsevier.com/materials-today-bio

IDH-genotype-linked kinase rewiring accompanies enhanced therapeutic response to dual-drug ferritin nanocages in high-grade glioma

Mara Schietinger [a], Sabri E.M. Sahnoun [b,c], Edda J. Krug [a], Philipp N. Loewe [a], Paolo Alimonti [c,d], Emiel P.C. van der Vorst [e,f], Najaf Mammadbayli [b], Agnieszka Morgenroth [b], Daniel Müller [g], Eva M. Buhl [h], Alaa A. Gad [a,b], Bernd Neumaier [i,j], Felix M. Mottaghy [b,k], Jörg B. Schulz [a,l], Katherine A. Vallis [c], Pardes Habib [a,m,*]

[a] Department of Neurology, University Hospital Aachen, RWTH Aachen University, Aachen, 52074, Germany
[b] Department of Nuclear Medicine, University Hospital Aachen, RWTH Aachen University, Aachen, 52074, Germany
[c] Department of Oncology, University of Oxford, Oxford, OX3 7DQ, United Kingdom
[d] Department of Neurosurgery, Brigham and Women's Hospital, Harvard Medical School, Boston, MA, 02120, USA
[e] Department of Internal Medicine I, Aachen-Maastricht Institute for Cardio-Renal Disease (AMICARE), and Institute for Molecular Cardiovascular Research (IMCAR), University Hospital Aachen, RWTH Aachen University, Aachen, Germany
[f] Institute for Cardiovascular Prevention (IPEK), Ludwig-Maximilians-Universität, Munich, Germany
[g] Interfaculty Chair of Neurobiology, Clinic for Neurology, RWTH Aachen University Medicine (UKA) and Institute for Biology 2, Faculty for Mathematics, Computer and Natural Sciences, Aachen, Germany
[h] Electron Microscopy Facility, Institute of Pathology, University Hospital Aachen, RWTH Aachen University, Aachen, 52074, Germany
[i] Institute of Radiochemistry and Experimental Molecular Imaging, University Hospital Cologne, University of Cologne, Cologne, 50937, Germany
[j] Institute of Neuroscience and Medicine, Forschungszentrum Jülich GmbH, Jülich, 52425, Germany
[k] Department of Radiology and Nuclear Medicine, Maastricht University Medical Center, Maastricht, 6202, the Netherlands
[l] JARA-BRAIN Institute of Molecular Neuroscience and Neuroimaging, Forschungszentrum Jülich GmbH and RWTH Aachen University, Aachen, 52074, Germany
[m] Department of Neurosurgery and Stanford Stroke Center, Stanford University School of Medicine, Stanford, CA, 94305, USA

ARTICLE INFO

Keywords:
Protein nanocarrier
Blood-brain barrier
Glioblastoma
Chemotherapeutic payload
PET
Imaging
Kinase signaling

ABSTRACT

Therapeutic resistance and limited brain penetration remain major challenges in high-grade gliomas. Protein-based nanocarriers, such as the heavy chain of human ferritin (FTH1), facilitate transferrin receptor-mediated transport across the blood-brain barrier. Here, we present multifunctional FTH1 nanocages as a unified nano-platform for dual-drug chemotherapy and molecular imaging. The nanocages achieve > 98 % gallium-68 labeling efficiency and enable pH-responsive release of doxorubicin and paclitaxel. In isocitrate dehydrogenase (IDH)-wildtype and IDH-mutant tumor models in ovo, FTH1 nanocages exhibit robust intracerebral distribution, tumor accumulation, and enhanced therapeutic efficacy. Dual-drug nanocages significantly reduce tumor growth ($p < 0.001$), with a stronger effect in the IDH-mutant model ($p < 0.001$), and improve embryo survival. Kinomic profiling reveals broad suppression of AGC and CMGC kinase families, consistent with attenuation of pro-survival and cell-cycle signaling, particularly in IDH-mutant models. These findings suggest treatment-associated kinase network adaptation linked to the IDH status of the models, consistent with increased therapeutic vulnerability, and support further evaluation of FTH1 nanocages as a platform for improved glioma treatment.

* Corresponding author. Department of Neurosurgery and Stanford Stroke Center, Stanford University School of Medicine, 1201 Welch Road, MSLS P352, Stanford, CA, 94305-5487, USA.

E-mail addresses: mara.schietinger@rwth-aachen.de (M. Schietinger), sabri.sahnoun@oncology.ox.ac.uk (S.E.M. Sahnoun), edda.krug@rwth-aachen.de (E.J. Krug), philipp.loewe@rwth-aachen.de (P.N. Loewe), palimonti97@gmail.com (P. Alimonti), evandervorst@ukaachen.de (E.P.C. van der Vorst), nmammadbayli@ukaachen.de (N. Mammadbayli), amorgenroth@ukaachen.de (A. Morgenroth), damueller@ukaachen.de (D. Müller), ebuhl@ukaachen.de (E.M. Buhl), agad@ukaachen.de (A.A. Gad), b.neumaier@fz-juelich.de (B. Neumaier), fmottaghy@ukaachen.de (F.M. Mottaghy), jschulz@ukaachen.de (J.B. Schulz), katherine.vallis@oncology.ox.ac.uk (K.A. Vallis), phabib@stanford.edu (P. Habib).

https://doi.org/10.1016/j.mtbio.2026.103539
Received 13 May 2026; Received in revised form 24 July 2026; Accepted 6 August 2026
Available online 6 August 2026
2590-0064/© 2026 The Authors. Published by Elsevier Ltd. This is an open access article under the CC BY license (http://creativecommons.org/licenses/by/4.0/).
Open access funding enabled and organized by Projekt DEAL.

1. Introduction

Glioblastoma (GBM) represents the most aggressive form of primary brain tumors, marked by rapid proliferation, diffuse infiltration, and, in most cases, inevitable recurrence despite maximal surgical resection and chemoradiotherapeutic intervention [1–3]. Median survival for isocitrate dehydrogenase-wildtype (IDH^{wt}) GBM remains approximately 15 months [2,4], whereas IDH-mutant (IDH^{mut}) high-grade gliomas show prolonged survival but ultimately develop therapy resistance [5–8]. Two major barriers hinder therapeutic progress in high-grade gliomas: their molecular adaptability, which contributes to intrinsic resistance, and the blood-brain barrier (BBB), limiting drug delivery [9–12].

Nanomedicine offers a promising avenue to address both challenges by facilitating targeted, combined drug delivery across the BBB [13–15], as it restricts the passage of most chemotherapeutics [16–22]. Temozolomide, a bioavailable agent with BBB penetrance, can improve outcomes, but resistance develops rapidly, and the prognosis of high-grade gliomas remains dismal [23,24]. Doxorubicin (DOX), an anthracycline, intercalates DNA and inhibits topoisomerase II, while paclitaxel (PTX), a taxane, stabilizes microtubules and induces cell cycle arrest [25,26]. Both agents elicit cytotoxic responses in GBM cells but fail to cross the BBB efficiently, limiting their clinical use [27–29]. Encapsulation in nanocarriers has been shown to enhance drug stability, tumor uptake, and therapeutic effects, motivating the development of delivery strategies to increase BBB penetration, including osmotic disruption, focused ultrasound, and receptor-mediated targeted drug delivery systems [22, 30–34].

Among nanoparticle (NP) formulations, protein-based nanocarriers such as the human ferritin heavy chain (FTH1) nanocages have emerged as particularly attractive because they are biocompatible, biodegradable, and reported to undergo transferrin receptor 1 (TfR1) mediated transcytosis across the BBB, while TfR1 is abundant on tumor cells and brain endothelial cells [35–39]. Human ferritin preserves structural integrity during transcytosis and can encapsulate diverse payloads for controlled release within the central nervous system (CNS) [40,41]. However, large-scale production of FTH1 is limited due to its high costs. Knödler et al. reported that recombinant expression of FTH1 in *N. benthamiana* plants can provide a scalable and economical option [42]. FTH1 nanocages can be post-synthetically modified with bioorthogonal tags like fluorophores or radiometal chelators, enabling modular theranostic design *via* covalent bioconjugation.

Despite these advances, a critical gap remains: how does the glioma genotype, particularly the IDH mutation status, shape the molecular responses to nanotherapies? Although IDH^{mut} gliomas are generally more chemosensitive than their wild-type counterparts, the mechanistic basis for this differential response remains incompletely understood [7, 43]. Because kinase signaling rapidly adapts under therapeutic stress, profiling drug-induced changes at the level of kinase activity provides a sensitive readout of pathway rewiring and genotype-associated adaptation [44–46].

Here, we address this gap by engineering a multifunctional platform based on plant-derived FTH1 nanocages loaded with DOX or PTX and equipped with a 1,4,7-triazacyclononane-1,4,7-triacetic acid (NOTA) *via* amine coupling for β^+-emitter (^{68}Ga) radiolabeling. This enables simultaneous dual-drug chemotherapy and positron emission tomography-computed tomography (PET/CT) imaging. We characterize uptake, trafficking, and cytotoxicity of FTH1 nanocages in U87-based glioma models differing in IDH-mutation status, providing a controlled comparative system with otherwise shared genetic background. Furthermore, we evaluate their biodistribution, intracerebral distribution, and therapeutic efficacy in the chorioallantoic membrane (CAM) xenograft model [47]. By integrating phenotypic readouts with kinomic profiling, we further characterize genotype-associated signaling adaptations induced by combination nanotherapy at the systems level. This approach enables comparative analysis of kinase network rewiring in IDH^{wt} and IDH^{mut} tumor models and provides insights into differential therapeutic response programs beyond conventional efficacy assessment.

Together, this work establishes a multifunctional FTH1 nanocage platform for combined drug delivery and molecular imaging and provides functional insight into treatment-associated kinase signaling adaptations in glioma models differing in IDH status.

2. Materials and methods

2.1. Formulation and functionalization of NPs

Recombinant human FTH1 nanocages were transiently produced in *N bethamania* by *R. radiobacter*-mediated vacuum infiltration and purified according to the protocol established by Knödler et al. [42]. The resulting purified FTH1 spontaneously assembles into spherical protein nanocages and served as the basis for all subsequent functionalization, radiolabeling, and drug loading experiments performed in this study. The same production batch was used in this study. Detailed physicochemical characterization of the FTH1 nanocages, including particle size distribution, structural integrity, and surface properties, has been previously reported [42]. In the present work, particle integrity and pH-dependent structural changes were additionally assessed by transmission electron microscopy (TEM).

2.1.1. Radiolabeling and stability of FTH1

FTH1 nanoparticles were functionalized with p-SCN-Bn-NOTA (2-S-(4-isothiocyanatobenzyl)-1,4,7-triazacyclononane-1,4,7-triacetic acid, Macrocyclics™, Plano, USA) by dissolving 0.1 mg NOTA in 100 µL ultrapure water, followed by the addition of 337.5 µg of FTH1 and 1 mL of ultrapure water. The mixture was incubated for 2 h at 37 °C under magnetic stirring. Radiolabeling was performed by incubating FTH1-NOTA at 37 °C for 30 min with 3 M NH_4OAc and ^{68}Ga, diluted in 0.6 M HCL. After adding cell culture medium, the pH was adjusted to 7.0 using 1 M NaOH.

Radiolabeling purity was assessed by radio-thin-layer chromatography (radio-TLC). 2 µL of the radiolabeling mixture was spotted onto TLC plates (Merck Silica F254, Sigma-Aldrich, Taufkirchen, Germany) and developed in sodium citrate buffer to a solvent front of 90 mm. Plates were analyzed using a radio detector (miniGita, Elysia-raytest, Angleur, Belgium).

For stability assessment, 20 µL of ^{68}Ga-FTH1 were incubated with 180 µL of phosphate-buffered saline (PBS) or human serum (HS) at 37 °C. HS were obtained from three healthy adult female and three healthy adult male donors. At 30-min intervals up to 180 min, 2 µL samples were withdrawn and analyzed by radio-TLC.

2.1.2. Negative staining of FTH1

To visualize extracellular degradation, FTH1 cages were prepared at pH 7.4 and pH 5.0 in the presence of 10 % glycerol. Samples were allowed to adsorb on glow-discharged formvar-carbon-coated nickel grids (Maxtaform, 200 mesh, Science Services GmbH, Munich, Germany) for 5 min. Negative staining was performed with 0.5 % uranyl acetate (in aqua dest., Science Services GmbH, Munich, Germany). Grids were air-dried and imaged using a Hitachi HT7800 transmission electron microscope (Hitachi, Tokyo, Japan) operating at an acceleration voltage of 100 kV.

2.1.3. Drug loading

To load the nanocarriers with DOX and PTX (Selleckchem, Houston, USA), FTH1 [0.375 mg/mL in 10 % Glycerol] was mixed with the drug and citrate buffer. The pH was adjusted to 11.3 by adding 1 M NaOH. Subsequently, the pH was decreased over a total period of 90 min by stepwise addition of 0.6 M HCl every 9 min until pH 7.5 was reached, free drug was removed after centrifugation.

For qualitative assessment of DOX encapsulation, increasing concentrations of FTH1 were mixed with a constant concentration of DOX

[0.1 mM] using the same loading protocol. Free DOX diluted in buffer was used as a control. 50 μL from each solution were diluted in 150 μL ultrapure water and transferred to a 96-well plate, followed by a fluorescence measurement detecting emission from 520 to 650 nm using a microplate reader (Molecular Devices SpectraMax M3 Multi-Mode Microplate Reader, Marshall Scientific, Hampton, USA).

Encapsulation efficiency (EE) and loading capacity (LC) were determined after removal of unencapsulated drug. Free DOX in the filtrate was quantified by UV-Vis spectroscopy using an external calibration curve. Free PTX was quantified by reverse-phase HPLC (Chromolith FastGradient RP-18e, 50 × 3 mm I.D.) with UV detection at 227 nm. PTX samples and calibration standards were prepared in acetonitrile:water (50:50, v/v). Chromatographic separation was performed using water (mobile phase A) and acetonitrile (mobile phase B) at a flow rate of 1.5 mL/min with an injection volume of 20 μL. A linear gradient was applied from 95 % A/5 % B to 5 % A/95 % B over 13 min. All measurements were performed in triplicate. EE and LC were calculated according to the following equations:

$$EE\% = \frac{\text{Initial conc.} - \text{Free conc.}}{\text{Initial conc.}}\ x\ 100$$

$$LC\left(\frac{mg}{mg}\right) = \frac{\text{Wt encapsulated drug}}{\text{Wt ferritin nanocages}}$$

where Wt encapsulated is the amount of drug encapsulated within the ferritin nanocages, and Wt ferritin nanocages is the total amount of ferritin nanocages used in the loading experiment.

2.1.4. Drug release

DOX- or PTX-loaded FTH1 nanocages were transferred into a Float-A-Lyzer G2 dialysis device (20 kDa MWCO, Spectrum Laboratories Inc., CA, USA) and dialyzed against PBS (pH 7.4) or sodium acetate buffer (0.01 M, pH 5.0) at 37 °C under continuous agitation. For PTX release studies, both release media were supplemented with 10 % (v/v) acetonitrile. At predetermined time points (0.5, 1, 2, 4, 24, 48 h), 500 μL of the release medium were collected and replaced with an equal volume of fresh pre-warmed buffer. Released DOX was quantified by fluorescence spectroscopy using a Tecan microplate reader based on a calibration curve generated from DOX standards, whereas released PTX was quantified by HPLC using external calibration standards. Cumulative drug release was corrected for sample replacement and expressed as the percentage of initially encapsulated drug.

2.2. In vitro studies

2.2.1. Cell culture

U87 IDH^{wt} and U87 IDH^{mut} cells were purchased from CLS Cell Lines Service (Eppelheim, Germany). Cells were cultured in Dulbecco's modified Eagle's medium (DMEM, Pan Biotech, Aidenbach, Germany) supplemented with 10 % fetal bovine serum (FBS, Pan Biotech, Aidenbach, Germany) and 0.5 % penicillin/streptomycin [P06-07100 (P/S, Pan Biotech, Aidenbach, Germany)], yielding a final concentration of 50 μg/mL penicillin and 50 μg/mL streptomycin. Cultures were maintained at 37 °C in a humidified incubator with 5 % CO_2. Cells were subcultured every two days by trypsinization (Trypsin/EDTA, Pan Biotech, Aidenbach, Germany), followed by centrifugation (400 x g, 5 min, RT). The pellet was resuspended in complete medium and seeded on well dishes or coverslips for immunocytochemistry (ICC).

For cell counting, 20 μL of the resuspended cell suspension was mixed with 20 μL of 0.4 % Trypan Blue solution (Sigma-Aldrich, Taufkirchen, Germany) and loaded onto a smart slide (ibidi, Gräfelfing, Germany). Cell number and viability were determined using a cell counter (Roche Innovatis Cedex XS, Basel, Switzerland).

2.2.2. GFP-transfection

U87 IDH^{wt} and U87 IDH^{mut} cells were transfected with pEGFP-N1 Vector (Catalog #6085-1), which encodes green fluorescent protein (GFP). Plasmid DNA was purified using the GeneJET Gel Extraction and DNA Cleanup Micro Kit (Thermofisher, Waltham, USA) according to the manufacturer's protocol. Plasmid DNA was cut using Vspl and Eco31l (both Thermofisher, Waltham, USA). Cells were transfected with exogenous DNA *via* electroporation. Subsequently, the cells were cultured in the presence of Geneticin™ (G418 Sulfate, Gibco, Waltham, USA) for two weeks to select for GFP-expressing clones.

2.2.3. Immunocytochemistry

For immunocytochemistry (ICC), cells were cultivated on coverslips for 24 h and then fixed with 3.7 % paraformaldehyde (PFA) in PBS (Pan Biotech, Aidenbach, Germany). Coverslips were transferred into a humid chamber and blocked with a buffer containing 0.5 g bovine serum albumin (BSA, 0163.4, Roth, Karlsruhe, Germany) and 1 mL of FBS mixed with 49 mL of PBS. Primary antibody incubation targeting CD71 receptor (Transferrin Receptor, Monoclonal Antibody (OKT9 (OKT-9)), eBioscience™) was performed overnight at 4 °C in blocking solution. The following day, a secondary antibody (Goat anti-Mouse IgG, Alexa Fluor™ 594, Invitrogen, USA) diluted in BS was applied for 1 h at RT. Cell nuclei were counterstained with 4′, 6-diamidino-2-phenylindole (DAPI, Roth, Karlsruhe, Germany). Samples were imaged using a fluorescence microscope (Leica, Wetzlar, Germany).

2.2.4. Transmission electron microscopy

TEM was performed by first seeding 5 × 10^5 cells per well in 6-well plates and culturing them for 24 h. FTH1 (12.5 μg per well) was diluted in 250 μL medium and added to the cells for a 2 h incubation at 37 °C. After removing the supernatant, cells were washed with PBS, fixed for 1 h in 3 % glutaraldehyde in 0.1 M Soerensen's phosphate buffer, scraped from the tissue plate, and centrifuged. Cell pellets were embedded in 5 % low-melting agarose (Sigma-Aldrich, St. Louis, USA). Samples were washed in PBS, post-fixed in 1 % osmium tetroxide (OsO4, Roth, Karlsruhe, Germany) in 25 mM sucrose buffer (Merck, Darmstadt, Germany), and dehydrated in a graded ethanol series (30, 50, 70, 90, and 100 %) for 10 min each. The final step (100 %) was repeated three times. Dehydrated specimens were infiltrated with Epon resin (Serva, Heidelberg, Germany) by incubation in a 1:1 mixture of ethanol and resin for 1 h, followed by 1 h in pure resin. Samples were embedded in pure Epon and polymerized at 90 °C for 2 h. Ultrathin sections (90-100 nm) were cut using an ultramicrotome (Reichert Ultracut S, Leica, Wetzlar, Germany) with a diamond knife (Leica) and picked up on HR23 Maxtaform Cu/Rh grids. Sections were stained with 0.5 % uranyl acetate and 1 % lead citrate (both EMS and Munich, Germany). Imaging was performed at an acceleration voltage of 60 kV using a Zeiss Leo 906 (Carl Zeiss, Oberkochen, Germany) transmission electron microscope.

2.2.5. Quantitative uptake studies

Cellular uptake of FTH1 was quantified by radioactivity measurements using a γ-counter (Wizard2, Perkin Elmer, MA, USA). U87 cell lines were cultured in 24-well plates at a density of 1 × 10^5 cells per well. Each well was treated with 0.65 μg of ^{68}Ga-FTH1 in 250 μL cell culture medium and incubated at 37.5 °C for 1 or 4 h. Afterward, the supernatant was removed, and cells were washed with PBS, trypsinized, and collected in γ-counter. tubes. Radioactivity was measured using a γ-counter calibrated for ^{68}Ga. Experiments were performed in triplicate, and cellular uptake was expressed as average counts per minute (A_{av}). Background radiation was determined using an empty γ-counter tube (BG). The percentage of NP incorporation was calculated relative to a reference sample (250 μL of ^{68}Ga-FTH1 medium) according to the decay-corrected formula:

$$NP_U[\%] = \frac{\frac{A_{av}}{e^{-0.010193341 \cdot t}} - BG}{ref} \cdot 100\%$$

2.2.6. Immuno electron microscopy

U87 cells were incubated with FTH1 nanoparticles for 90 min, subsequently fixed in 4 % PFA, and embedded in HM20 *via* freeze substitution after high-pressure freezing. Freeze substitution was performed with methanol dehydration steps at -90 °C and ethanol dehydration steps at -50 °C up to 0 °C. Polymerization was done at -50 °C under UV light. Immune labeling was performed on ultrathin sections. Sections underwent antigen retrieval in citrate buffer (Vector Laboratories, Newark, USA) at 98 °C for 20 min. After blocking with 5 % BSA, the primary antibody against FTH1 (Antibodies online, Aachen, Germany) was incubated at a concentration of 1:20 in 1 % BSA/PBS overnight at 4 °C. A secondary antibody labeled with 12 nm gold particles was incubated for 4 h. Contrast was enhanced by staining with 0.5 % uranyl acetate and 1 % lead citrate (both EMS, Munich, Germany). Samples were examined using a Hitachi HT7800 transmission electron microscope (Hitachi, Tokyo, Japan) operating at an acceleration voltage of 100 kV.

2.2.7. Cell viability assessments

Cell viability was assessed by measuring lactate dehydrogenase (LDH) release into the culture medium using the CytoTox 96® Non-Radioactive Cytotoxicity Assay (#G1782, Promega, Madison, WI, USA), according to the manufacturer's protocol. For positive control, 25 µL lysis solution (Triton-X) was applied to the cells and incubated for 30 min before measurement. Supernatants (50 µL) were transferred to a 96-well plate, and 50 µL assay reagent was added to each well. In addition, a media-only control was included for background correction. Absorbance was recorded at 490 nm using a microplate reader (Tecan GmbH, Mannedorf, Switzerland).

Cell metabolic activity was evaluated with the Cell Titer-Blue® Cell Viability Assay (Promega, Madison, WI, USA), following the manufacturer's protocol. After removal of the medium, 200 µL of reagent-medium mixture (1:20 ratio) was added per well. The reduction of resazurin to fluorescent resorufin requires functional mitochondrial respiration and occurs only in viable cells. After 1 h incubation, 100 µL of the supernatant was transferred to a 96-well plate for fluorescent measurement ($\lambda_{ex} = 560$ nm and $\lambda_{em} = 590$ nm).

For all experiments, 5×10^4 cells were seeded in 24-well plates 24 h before treatment. DOX and PTX were loaded onto FTH1 as described and added to 250 µl medium at a concentration of 0.65 µg FTH1 per 5×10^4 cells. After 4 h incubation, particles were removed, and cells were washed with 300 µL PBS. Cells were maintained in 1 mL fresh medium at 37 °C until viability and metabolic measurements were performed. Each condition was evaluated in five independent biological experiments using independently cultured cell batches, with each biological replicate analyzed in three technical replicates.

2.2.8. Holo-transferrin competition assay

U87 IDH^{wt} and U87 IDH^{mut} cells were seeded into 96-well plates at a density of 1×10^4 cells per well and cultured under standard conditions until the day of the experiment. To assess the effect of holo-transferrin on ferritin nanocage uptake, cells were pre-incubated with 200 µg/mL holo-transferrin for 30 min at 37 °C. Following the pre-incubation period, Cy5-labeled FTH1 nanocages were added to a final concentration of 0.1 µM, while maintaining the holo-transferrin in the culture medium throughout the incubation period. Control cells were treated with 0.1 µM Cy5-labeled FTH1 nanocages alone under identical conditions without holo-transferrin pre-treatment. Cells were incubated for 1 h or 4 h at 37 °C. Following, the cells were washed twice with PBS to remove unbound nanocages. Cellular uptake of Cy5-labeled FTH1 nanocages was quantified using a Tecan Spark microplate reader (excitation 645 nm, emission 680 nm). Fluorescence intensities were converted into cell-associated FTH1 nanocage concentrations using a calibration curve generated from serial dilutions of Cy5-labeled nanocages with known concentrations.

2.3. In ovo studies

2.3.1. In ovo tumor growth model

For the ectopic tumor growth model, fertilized LSL chicken eggs (LOHMANN Deutschland GmbH & Co. KG, Ankum, Germany) were incubated at 37.8 °C and 60 % humidity (Type Easy 250, J. Hernel Brutgeräte GmbH & Co. KG, Verl, Germany). On incubation day 5, a rectangular viewing window was cut into the eggshell and sealed with scotch tape. On day 9, a silicone ring was placed on the CAM, and the membrane was gently scratched using a cannula. Per egg, 2×10^6 U87 cells were mixed with Matrigel® matrix (Corning, Fisher Scientific GmbH, Schwerte, Germany) and applied into the ring.

Survival and tumor growth were monitored every two days. Images were acquired using a light microscope (Leica A60, Wetzlar, Germany). A Kaplan-Meier survival curve was generated and analyzed using GraphPad Prism (version 10.2.3, San Diego, CA, USA).

2.3.2. Imaging and biodistribution

To constitute the biodistribution *in ovo*, ^{68}Ga-FTH1 (10 MBq per embryo) was mixed with 60 µL of contrast agent (Ultravist-300®, 300 mg iodine/ml, Bayer AG, Leverkusen, Germany) and 15 µL Trypan Blue. Chicken embryoss were anesthetized with 1.5 % isoflurane in oxygen (0.8 L/min) for 3 min prior to intravenous injection using a 32G needle. Imaging was performed with a small animal PET/CT system (X-CUBE and ß-CUBE, Molecubes, Gent, Belgium). After 10 min incubation, a high-resolution CT scan was initiated (5 min, 440 µA, 50 kVp, 32 ms exposure, 1080° spiral rotation), followed by a 20 min PET scan. Isoflurane anesthesia was continued during the scans.

After imaging, embryos were sacrificed by decapitation and dissected. The brain, heart, liver, intestines, and the rest of the body were collected, and their radioactivity was measured using a γ-counter. Gamma counting data were normalized to organ weight and expressed as a percentage of total measured activity. For ARG, brains were perfused with PBS to remove residual blood, fixed in 3.7 % PFA, and cut into six (2 mm thick) coronal brain sections. Subsequently, three brain sections were placed on imaging plates (Fuji Film BAS-IP SR 2025, Raytest, Germany) for 24 h at RT and scanned using the Typhoon FLA 7000 (GE Healthcare, IL, USA) to visualize the distribution of ^{68}Ga-FTH1 NPs.

2.3.3. In ovo therapy

To investigate the therapeutic effect of drug-loaded FTH1 nanocages on ectopic IDH^{wt} and IDH^{mut} tumors, DOX or PTX were encapsulated into FTH1 nanocages. On incubation day 14, tumor-bearing embryos were randomly divided into two groups. Baseline tumor volumes were determined by CT imaging on day 14, and treatment response was assessed by follow-up CT imaging and tissue collection on day 19, defining the experimental observation interval. One group received FTH1[DOX + PTX], diluted in ultrapure water and mixed with 15 µL trypan blue, which was injected intravenously into the CAM. Drug doses were selected based on commonly reported ranges for orthotopic glioblastoma mouse models and scaled to embryo body weight (1 mg/kg = 1 µg/g) [29,48]. Chicken embryos at embryonic day 14 typically weigh approximately 10–15 g, depending on strain and incubation conditions [49]. Using a representative average weight of ~12 g, the calculated doses correspond to approximately 24 µg DOX and 48 µg PTX per embryo. For the dual-drug formulation, the total drug amount was distributed between both compounds, resulting in approximately 12 µg DOX and 24 µg PTX per embryo. For the control group, an equal volume of empty nanocages diluted in ultrapure water and trypan blue was injected. After dissection on day 19, tumor tissue was collected and stored at −80 °C for further analyses.

PET and CT scans were evaluated with PMOD (version 4.1., PMOD Technologies LLC, Fällanden, Switzerland) using the View and Fusion Tool. The CT scan was used as the anatomical reference, and PET images were rigidly coregistered to the CT. Fusion images were visually

inspected to ensure accurate anatomical alignment between PET and CT datasets. Tumor regions were segmented using a Volume of Interest (VOI) workflow. First, anatomical tumor boundaries were delineated manually on the CT images to avoid spill-in from adjacent structures. A consistent segmentation workflow was applied across all datasets to ensure comparability of tumor volume measurements. The investigator performing the segmentation was blinded to the treatment status of the samples during volumetric analysis. PMOD automatically calculated tumor volumes by summing up all voxels assigned to the VOI and multiplying by the corresponding voxel dimensions. Final tumor volumes were expressed in mm^3.

2.3.4. Quantitative reverse transcription PCR (qPCR)

Gene expression analysis was performed with tissue from the harvested organs or biopsies from ectopic tumors. RNA was isolated as previously described [50]. Concentration and quality were assessed using a Tecan plate reader, and samples were diluted to a concentration of 500 ng/µL. Complementary DNA (cDNA) synthesis was performed using the iScript™ cDNA Synthesis Kit (Biorad, Germany) according to the manufacturer's instructions. Real-time qPCR was carried out using the iQ™ SYBR® Green Supermix (Biorad, Germany) on a CFX Opus 96 Real-Time PCR System (Biorad, Germany). The target genes and one housekeeping gene (glyceraldehyde-3-phosphate dehydrogenase (GAPDH)) were measured at cycle threshold (CT) values, and relative quantities were analyzed using the ΔΔCT method with the qbase + software (Biogazelle, Belgium). A list of used primers, including sequences and annealing temperatures, is given in Table 2.

2.3.5. TUNEL and cleaved Caspase-3 staining

Tumors were collected, snap-frozen, and stored at -80 °C until cryosectioning. Cryosections (25 µm) were prepared using a cryostat and mounted onto microscope slides. For the cleaved-Caspase-3 staining, sections were blocked and incubated overnight at 4 °C with a rabbit anti-cleaved Caspase-3 (Asp175) primary antibody (Cell Signaling Technology, Danvers, MA, USA). After washing, sections were incubated for 1 h at RT with an Alexa Fluor™ 594-conjugated goat anti-rabbit IgG secondary (Invitrogen, Waltham, USA). Nuclei were counterstained with DAPI (Roth, Karlsruhe, Germany). TUNEL assay was performed using the In Situ Cell Death Detection Kit, Fluorescein (Roche, Mannheim, Germany) according to the manufacturer's protocol. Briefly, cryosections were fixed with 4 % PFA, permeabilized with 0.1 % Triton X-100/0.1 % sodium citrate, incubated with the TUNEL reaction mixture for 1 h at 37 °C, and counterstained with DAPI.

Samples were imaged using a fluorescence microscope (Olympus, Wetzlar, Germany). TUNEL fluorescence was quantified in Fiji (ImageJ, NIH). Whole tumor sections were manually delineated as regions of interest (ROIs), and the mean fluorescence intensity was determined for each section under identical image settings.

2.4. Kinase activity profiling

Kinase profiles were determined using the PamChip® peptide tyrosine kinase microarray system (PTK) or the PamChip® Serine/Threonine kinase assay (STK) on PamStation®12 (PamGene International, ′s-Hertogenbosch, The Netherlands). The phosphorylation of the peptides is visualized by detection of the fluorescent signal, which is emitted as a result of the binding of the FITC-conjugated PY20 anti-phosphotyrosine antibody. Punched probes of the tumor tissue were collected and washed once in ice-cold PBS after respective treatments, with 12-14 biological replicates per condition, and lysed for 15 min on ice using M-PER Mammalian Extraction Buffer containing Halt Phosphatase Inhibitor and EDTA-free Halt Protease Inhibitor Cocktail (1:100 each; Thermo Fischer Scientific). Lysates were centrifuged for 15 min at 16.000 x g at 4 °C in a pre-cooled centrifuge. Protein quantification was performed with Pierce™ Coomassie Plus (Bradford) Assay according to the manufacturer's instructions.

PTK and STK assays were performed using the standard protocol supplied by Pamgene and as previously described by van der Vorst et al. [51]. For PTK assays, 10 µg of protein per array were incubated in PTK reaction buffer containing ATP and FITC-conjugated anti--phosphotyrosine antibody. For STK assays, 2 µg of protein were incubated with ATP in the STK reaction mix. In both assays, lysates were applied to BSA-blocked arrays and processed on a PamStation®12 platform with kinetic imaging acquisition. Spot intensities were quantified and background corrected using BioNavigator software version 6.3 (PamGene International, ‘s-Hertogenbosch, The Netherlands). Upstream Kinase Analysis (UKA) [52], a functional scoring method (PamGene) was used to rank kinases based on combined specificity scores (based on peptides linked to a kinase, derived from 6 databases) and sensitivity scores (based on treatment-control differences).

Principal Component Analysis (PCA) was conducted to explore patterns of variation and clustering among samples based on peptide phosphorylation profiles. The analysis was performed using the stats package in R (R Foundation for Statistical Computing, Vienna, Austria), which applies singular value decomposition to the centered and scaled data matrix to examine covariances and correlations between samples. To visualize the results, the ggplot2 (Springer-Verlag, New York) was used to generate two-dimensional PCA plots, highlighting sample distribution along the principal components.

Kinase family distribution and classification were visualized using a coral kinase tree generated with the Coral web tool (http://phanstiel-lab.med.unc.edu/CORAL). Kinases detected as active in the PTK or STK PamChip® assays were grouped into their respective families according to the classification system provided by the Human Kinome Project. Node/branch colors represent mean kinase statistics (<0.05), and node sizes represent the median final scores (>1.2), enabling visualization of family-wide and condition-specific kinase activation patterns.

Over-representation analyses (ORA) of Gene Ontology for the kinases with significant differences from baseline were performed using the ClusterProfiler R-package [53]. The list of kinases of interest contains the kinases with higher median final scores (>1.2). For the GO enrichment analysis, we selected only the Biological Process (BP) terms and filtered out redundantly enriched GO terms by retaining only the terms with the lowest adjusted p-value among all redundant terms. The redundant terms were defined as the GO terms that have similarities higher than 0.7. The p-values were adjusted for multiple comparisons by false discovery rate.

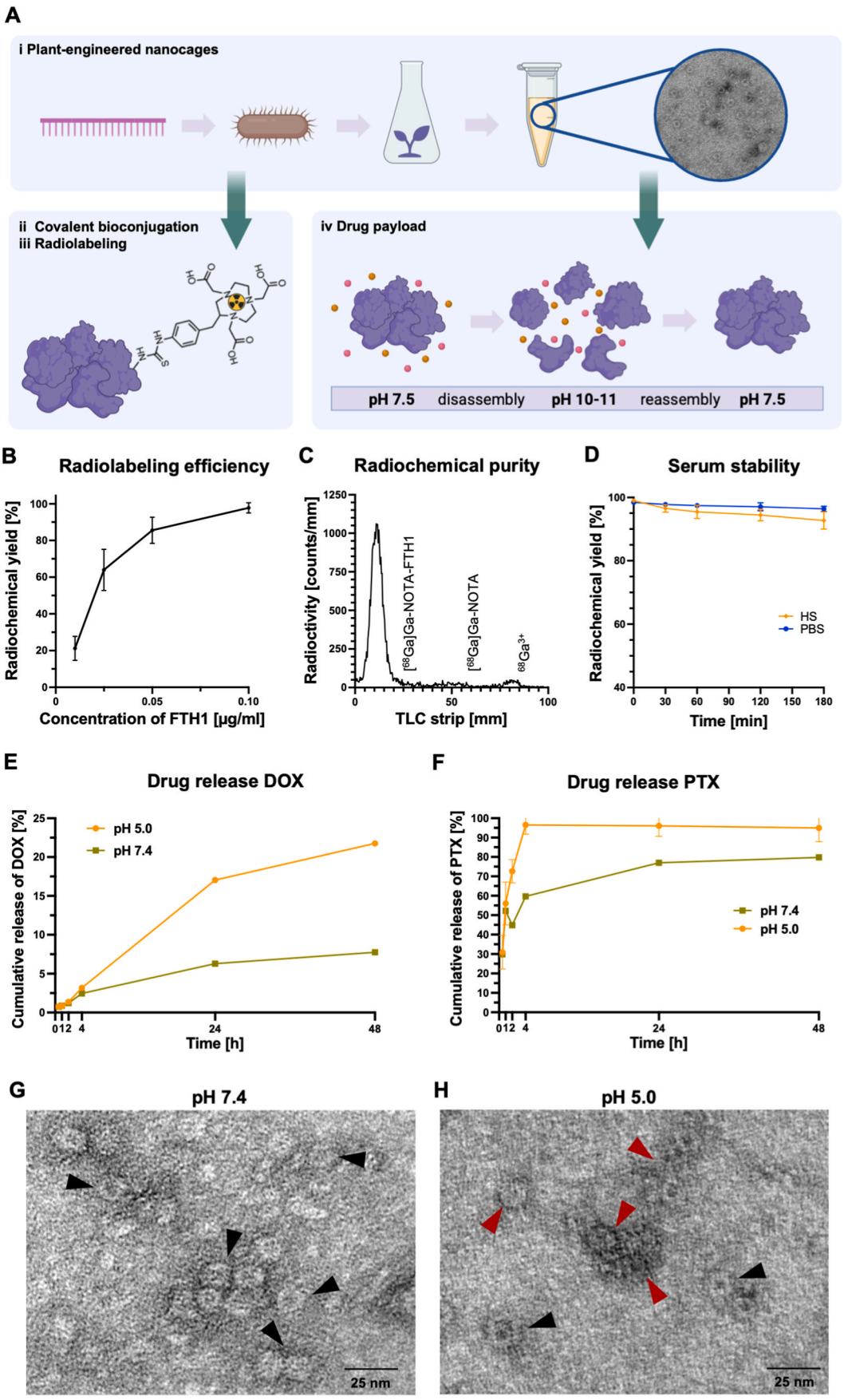
2.5. Statistics

Data analysis and visualization were performed using GraphPad Prism (version 10.3.1, San Diego, CA, USA). Data were first assessed for normal distribution using the Shapiro-Wilk test. Depending on the data structure, intergroup differences were analyzed using ANOVA one-way or two-way, followed by *Tukey's post hoc test* or by *Kruskal-Wallis test* for non-parametric data. For pairwise comparisons, an unpaired *t*-test or *Mann-Whitney tests* were applied. Boxplots show the median with interquartile range and whiskers representing the full data range. Data are given as arithmetic means ± SD. $P < 0.033$ was considered statistically significant after correction for multiple testing. The number of experimental and technical repeats is indicated in the corresponding figure legends, including the statistical tests employed.

3. Results

3.1. Multifunctional FTH1 nanocages achieve efficient, stable radiolabeling and enable controlled pH-responsive release through degradation

The design strategy of our multifunctional theranostic platform is based on recombinant human FTH1 nanocages transiently produced in *N. benthamiana* by *R. radiobacter*-mediated vacuum infiltration and



(caption on next page)

Fig. 1. Chemical functionalization, stability, drug loading, and pH-responsive release behavior of FTH1 nanocages (A) Schematic design of plant-engineered FTH1 nanocages, **(ii)** their covalent bioconjugation with the radiometal chelator NOTA, **(iii)** radiolabeling with PET imaging radionuclides, **(iv)** and their pH-dependent drug loading. **(B)** Concentration-dependent radiolabeling efficiencies of ^{68}Ga-FTH1 are shown using radio-TLC. **(C)** A representative radio-TLC chromatogram demonstrating the radiochemical purity (RCP) of ^{68}Ga-FTH1. **(D)** To evaluate the stability of ^{68}Ga-FTH1, time-dependent measurements in HBS or PBS control were performed. Data are shown as mean ± SD of 3 independent experiments with 3 technical replicates. (**E-F**) pH-dependent drug release from FTH1 nanocages. (**E**) Cumulative release of DOX and (**F**) cumulative release of PTX from FTH1 nanocages under physiological (pH 7.4) and acidic (pH 5.0) conditions over 48 h. Data are presented as mean ± SD from two independent experiments. (**G, H**) Representative negatively stained TEM images illustrating the pH-dependent structural integrity of extracellular FTH1 nanocages at pH 7.4 (G) or 5.0 (H). Black arrows point to intact, red arrows to disrupted nanocages. (For interpretation of the references to color in this figure legend, the reader is referred to the Web version of this article.)

purified as previously described [42]. Following purification, the FTH1 subunits self-assemble into spherical nanocages that inherently target TfR1-expressing cells and serve as the basis for subsequent functionalization and drug loading(Fig. 1A). Covalent bioconjugation with NOTA allowed radiolabeling with β^+-emitter ^{68}Ga for PET imaging (Fig. 1A). Subsequently, the FTH1 nanocages were loaded with DOX or PTX as cytostatic payloads through a pH-dependent disassembly/reassembly strategy (Fig. 1A). To quantitatively characterize drug loading, EE and LC were determined for both chemotherapeutics (Fig. S1B). DOX exhibited an EE of 78.48 ± 2.09 % with a LC of 0.944 ± 0.004 mg drug/mg ferritin, whereas PTX showed an EE of 54.53 ± 13.54 % with a LC of 0.144 ± 0.03 mg drug/mg ferritin. These quantitative measurements are complemented by the fluorescence-based loading analysis (Fig. S1A). The radiometal chelator NOTA was attached covalently *via* bioconjugation to FTH1 (NOTA-FTH1), enabling the incorporation of imaging moieties into the platform. ^{68}Ga (t ½ = 68 min) was used for radiolabeling to synthesize [^{68}Ga]Ga-NOTA-FTH1 (^{68}Ga-FTH1) for PET imaging. Utilizing radio-TLC, the radiolabeling efficiency of ^{68}Ga-FTH1 demonstrated radiochemical yields (RCY) of ≥ 95 % at NOTA-FTH1 concentrations of ≥ 0.1 μg/mL (Fig. 1B). Representative radio-TLC chromatograms confirmed radiochemical purities of ≥ 95 % for ^{68}Ga-FTH1, indicating successful chelation of ^{68}Ga and stable NOTA attachment (Fig. 1C). To determine the serum stability of ^{68}Ga-FTH1 in HS or PBS control, radio-TLCs were performed in a time-dependent manner, showing RCYs of around 92 % in HS and around 96 % in PBS after 3 h at 37 °C (Fig. 1D). To further characterize the drug delivery properties of FTH1 nanocages, cumulative release profiles were evaluated under physiological (pH 7.4) and acidic (pH 5.0) conditions over 48 h using a dialysis-based release assay (Fig. 1E and F). DOX exhibited a sustained and pH-dependant release profile, reaching approximately 21 % cumulative release at pH 5.0 compared with 7 % at pH 7.4 after 48 h (Fig. 1E). Similarly, PTX release was higher under acidic conditions, reaching approximately 95 % at pH 5.0 compared with 76 % at pH 7.4 after 48 h (Fig. 1F). These findings were supported by negatively stained TEM imaging (Fig. 1G and H), showing intact spherical extracellular nanocages under pH 7.4 (Fig. 1G, black arrows), whereas acidic conditions (pH 5.0) led to pronounced structural disruption of the nanocages (Fig. 1H, red arrows). This structural destabilization is consistent with the increased drug release observed under acidic conditions.

In conclusion, our integrated platform enables image-guided multitherapeutic drug delivery and provides a foundation for subsequent biological evaluation.

3.2. *IDH^{mut} glioma cells exhibit enhanced intracellular FTH1 uptake, accompanied by endolysosomal accumulation*

To characterize the intracellular uptake dynamics of FTH1 nanocarriers in U87 cells, we performed complementary *in vitro* experiments (Fig. 2). Immunocytochemistry confirmed expression of the transferrin receptor CD71 in both U87 IDH^{wt} and U87 IDH^{mut} cells, confirming the presence of the molecular target of FTH1 nanocages and thereby providing the biological rationale for subsequent experiments. Fluorescence signals were predominantly localized to the plasma membrane and within the cytoplasm (Fig. 2A).

To assess the efficiency and kinetics of cellular internalization, intracellular uptake of ^{68}Ga-FTH1 was quantified in U87 cells, after 1 h and 4 h incubation time (Fig. 2D). In both cell lines, uptake increased significantly ($p < 0.033$) over time, doubling between the two time points with an average increase from 1.5 % to 3 % in IDH^{wt} and 2 % to 4 % in U87 IDH^{mut} between 1 h and 4 h. Uptake was higher in IDH^{mut} cells ($p < 0.033$), suggesting IDH-status-associated differences in NP internalization. Competitive uptake experiments further showed that holo-transferrin preincubation significantly reduced FTH1 nanocage uptake in both cell lines (Fig. S2A).

TEM demonstrated distinct FTH1 nanocages within endolysosomal compartments of U87 glioma cells independently of their IDH-mutation status (Fig. 2C–E). Furthermore, distinct stages of structural dispersion were observed, consistent with progressive intracellular nanocage degradation, with more intact nanocages (dark blue arrow) in peripheral lysosomes and increasingly fragmented structures (light blue arrow) in perinuclear compartments (Fig. 2E).

To validate nanoparticle identity at the ultrastructural level, immunogold-TEM with anti-FTH1 antibodies confirmed the intracellular presence of FTH1 NPs (Fig. 2G). Besides a native intracellular amount of FTH1, immune TEM revealed a significantly ($p < 0.001$) higher number of particles per cell section compared to untreated controls.

In summary, these results indicate efficient internalization of FTH1 nanocages in both U87 cell lines, with predominant trafficking into endolysosomal compartments and higher uptake in IDH^{mut} cells.

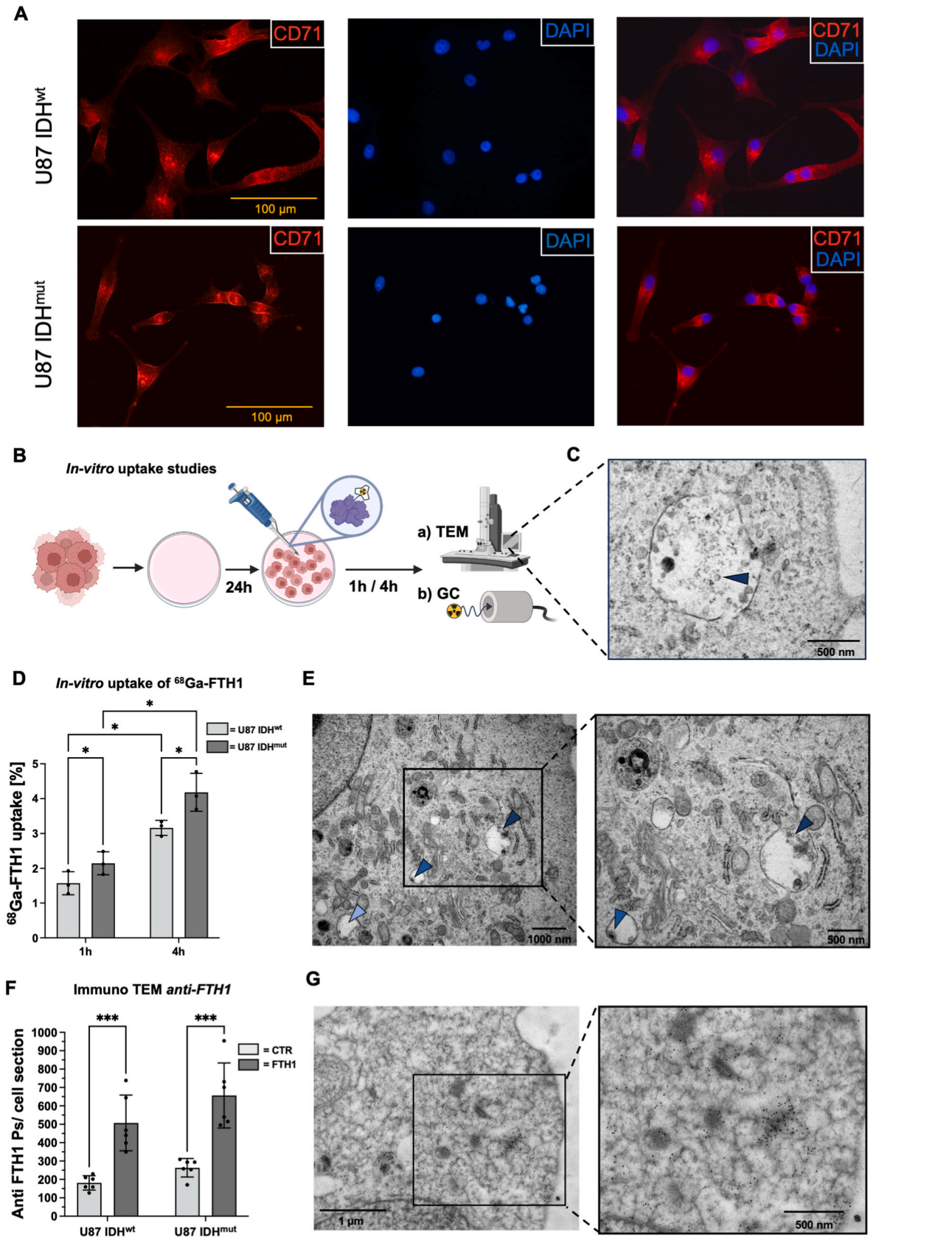
3.3. *Dual-drug FTH1 nanocarriers reduce metabolic activity and induce cell death in glioma cells*

To evaluate the time-dependent therapeutic effects of drug-loaded nanocarriers and the intrinsic toxicity of FTH1 NPs, we exposed U87 cell lines to free drugs or NP formulations (FTH1[drug]) for 4 h, followed by longitudinal viability and metabolic assays (Fig. 3A and B).

Treatment with bare FTH1 consistently resulted in LDH release below 10 % across all time points and in both genotypes, with no significant difference compared to the untreated vehicle control (Fig. 3A), indicating negligible intrinsic toxicity. In contrast, exposure to drug-loaded NPs induced a marked increase in LDH release (>20 %), indicative of increased cytotoxicity.

Metabolic activity, measured by CTB assay, was significantly reduced in cells treated with FTH1[DOX] and FTH1[DOX + PTX] compared to bare NPs (Fig. 3B). For both genotypes and across all time points, FTH1[DOX] led to a stronger decline (8-25 % residual activity) than FTH1[PTX] (29-38 %). Among the tested formulations, the combined formulation, FTH1[DOX + PTX], produced the greatest reduction in metabolic activity to 5-15 %. This observation was consistent for both genotypes, with a trend to lower residual activity in IDH^{mut} cells. A progressive reduction in metabolic activity was detected over time, with the lowest levels at 96 h (8 % in IDH^{wt} and 6 % in IDH^{mut} cells), indicating a sustained therapeutic effect of the encapsulated drugs. Furthermore, no significant differences were observed between free drugs and their NP-encapsulated counterparts, indicating that nanoparticle encapsulation preserved the cytotoxic activity of the respective treatments.

Together, these findings demonstrate that dual-drug FTH1 nanocages induce a greater cytotoxic effect than the corresponding single-drug



(caption on next page)

Fig. 2. Intracellular uptake and ultrastructural localization of FTH1 nanocages in U87 glioma cells. **(A)** Representative immunocytochemistry of CD71 (red) and nuclear staining with DAPI (blue) in U87 IDH^{wt} and U87 IDH^{mut}. (**B**) Schematic workflow of uptake studies. **(C)** TEM image showing intracellular localization of FTH1 within endolysosomal structures (blue arrow). **(D)** Quantification of time-dependent cellular uptake of ^{68}Ga-FTH1 in U87 IDH^{wt} and U87 IDH^{mut} after 1 h or 4 h incubation by gamma counting. Bars represent means ± SD of 3 independent experiments with 3 technical replicates. A two-way ANOVA followed by *Tukey's post hoc test* was performed, *p < 0.033; **p < 0.01; ***p < 0.001; ns, not significant (**E**) TEM images visualizing intracellular dispersion of FTH1 nanocages. Arrows show nanocages in different dispersion stages. (**F**) Quantification of Immunogold-TEM after treatment with FTH1 NPs and staining with FTH1 antibodies, visualizing the number of gold particles (Ps) on U87 IDH^{wt} and U87 IDH^{mut}. Bars represent means ± SD of 6 individual cell sections. A two-way ANOVA followed by *Tukey's post hoc test* was performed. *p < 0.033; **p < 0.01; ***p < 0.001; ns, not significant. (**G**) Representative TEM after immunogold staining with FTH1 antibodies. (For interpretation of the references to color in this figure legend, the reader is referred to the Web version of this article.)

formulations under the experimental conditions tested, thereby supporting their further evaluation *in vivo*.

3.4. *In ovo PET/CT imaging demonstrates intracerebral distribution and tumor accumulation of ^{68}Ga-FTH1 nanocages*

To characterize the systemic biodistribution of our multifunctional ^{68}Ga-FTH1 platform, we employed the CAM model as an *in ovo* screening platform enabling assessment of systemic distribution, intracerebral exposure, and tumor accumulation. The ectopic CAM tumor model was established using fertilized chicken embryos (Fig. 4A), providing a cost-efficient, rapidly developing system suitable for high-throughput analysis. Optimization of tumor cell seeding and membrane handling yielded a reproducible tumor formation rate of 80-90 %.

For proof of concept, we implanted GFP-transfected U87 glioma cells onto the CAM, enabling non-invasive fluorescence-based tumor detection (Fig. 4B). Ectopic tumors developed as compact, vascularized masses on the CAM, visible under both bright-field (Fig. 4B, upper) and fluorescence (Fig. 4B, lower) imaging. Serial macroscopic imaging over 9 days demonstrated progressive tumor expansion, monitored using a fixed silicon reference ring (Fig. 4C).

To investigate systemic distribution of ^{68}Ga-FTH1 nanocages *in ovo*, PET/CT imaging was performed 20 min after intravenous injection. Representative scans showed distinct systemic intra-embryonic tracer distribution (Fig. 4D). High PET signal intensities were observed in the thoracic and abdominal region (red signal, left and middle panels), corresponding to highly perfused organs like the heart, large vessels, or liver. Importantly, a focal signal was detected in the cranial region, indicating intracerebral distribution and presence of the nanocages (Fig. 4D left and middle panel).

These imaging findings were further substantiated by organ-level activity measurement using gamma counting of dissected organs 1 h after injection(Fig. 4E–G). At this time point, the highest activity was localized in the liver (~55 %), consistent with hepatic processing of FTH1. Notably, approximately 6 % of activity was detected in the brain, indicating measurable intracerebral presence of ^{68}Ga-FTH1. Autoradiography of coronal brain sections confirmed homogeneous intracerebral signal distribution (Fig. 4F).

In tumor-bearing embryos, merged PET/CT images revealed a distinct focal hotspot at the ectopic tumor site (Fig. 4D, right panel), indicating tumor accumulation of the nanocages.

Collectively, these findings indicate systemic bioavailability of ^{68}Ga-FTH1 nanocages, detectable intracerebral distribution in the embryo, and accumulation in ectopic U87 glioma xenografts and motivate subsequent evaluation of *in ovo* therapeutic efficacy.

3.5. *Dual-drug FTH1 nanotherapy suppresses tumor growth and is associated with pro-apoptotic transcriptional changes in IDH^{mut} tumors*

To assess the therapeutic efficacy of our dual drug-loaded nanoparticles, ectopic U87 IDH^{mut} and IDH^{wt} tumors established on the CAM were treated on day 15 with FTH1 [DOX + PTX] and analyzed on day 19 (Fig. 5).

Kaplan-Meier analysis demonstrated that FTH1 [DOX + PTX] treatment improved embryo survival compared to untreated tumor-bearing controls (Fig. 5A). In embryos harboring IDH^{wt} tumors, survival increased from 71 % to 93 % following treatment. Similarly, survival of embryos carrying IDH^{mut} tumors improved from 68 % to 87 %.

Tumor growth dynamics, quantified by serial CT imaging, further supported these observations (Fig. 5B). Untreated tumors displayed an increase in volume between days 14 and 19, with IDH^{mut} tumors growing more rapidly than their IDH^{wt} counterparts ($p < 0.001$). FTH1 [DOX + PTX] treatment significantly suppressed rapid tumor expansion in both genotypes ($p < 0.01$ vs controls). Notably, the magnitude of growth inhibition was significantly greater in treated IDH^{mut} tumors ($p < 0.001$ compared to treated IDH^{wt} tumors), consistent with increased treatment sensitivity.

Transcriptional analysis utilizing qPCR supported these observations (Fig. 5C–E). The pro-apoptotic marker Bax was significantly upregulated in both IDH-genotypes after treatment ($p < 0.01$, $p < 0.001$), with a more pronounced increase in IDH^{mut} tumors (Fig. 5D). In contrast, expression of the anti-apoptotic gene Bcl2 remained largely unchanged (Fig. 5C), while the inflammatory marker IL1-β was reduced upon therapy (Fig. 5E). To further assess apoptosis at the tissue level, tumor cryosections were analyzed by TUNEL staining and cleaved-Caspase-3 immunofluorescence. Compared with FTH1-treated controls, FTH1 [DOX + PTX] treatment resulted in increased TUNEL signal in both IDH^{wt} and IDH^{mut} tumors (Fig. 5F). Quantitative analysis confirmed a significant increase in mean TUNEL intensity following treatment in both genotypes ($p < 0.01$ for IDH^{wt}; $p < 0.001$ for IDH^{mut}; Fig. S3F). Consistent with these findings, treated tumors also exhibited increased cleaved Caspase-3 immunostaining (Fig. S3D and E). Additional analysis of peripheral embryonic tissue (Fig. S3A–C) revealed no widespread activation of apoptotic markers across the organs, indicating limited systemic toxicity.

These findings show that dual drug-loaded FTH1 nanocages improve embryo survival and substantially suppress tumor growth in ectopic U87 CAM tumors. Notably, tumor growth inhibition was more pronounced in the IDH^{mut} model, consistent with increased therapeutic sensitivity. These observations motivated further investigation of treatment-associated signaling adaptations using kinomic profiling.

3.6. *Kinase activity profiling identifies differential suppression of AGC and CMGC-family kinases in IDH^{mut} tumors following FTH1 [DOX + PTX] therapy*

To characterize treatment-associated kinase signaling responses in tumors differing in IDH status, we performed kinase activity profiling in ectopic IDH^{wt} and IDH^{mut} tumor xenografts with or without FTH1 [DOX + PTX] therapy (Fig. 6).

Analysis of significantly regulated kinases demonstrated distinct kinase response patterns between genotypes (Fig. 6A). In IDH^{wt} tumors, therapy markedly increased the number of upregulated kinases (WT DP vs WT), suggesting activation of compensatory signaling. In contrast, IDH^{mut} tumors exhibited a predominantly suppressive kinase profile (Mut DP vs Mut). The largest set of downregulated kinases was observed in the Mut DP vs WT DP comparison, indicating a substantial genotype-associated divergence in therapy-induced signaling output.

PCA further highlighted these distinctions (Fig. 6B). While untreated samples clustered closely, indicating broadly similar baseline kinase activity states, therapy induced a clear separation. PTK activity was significantly altered in treated wildtype tumors, whereas STK activity

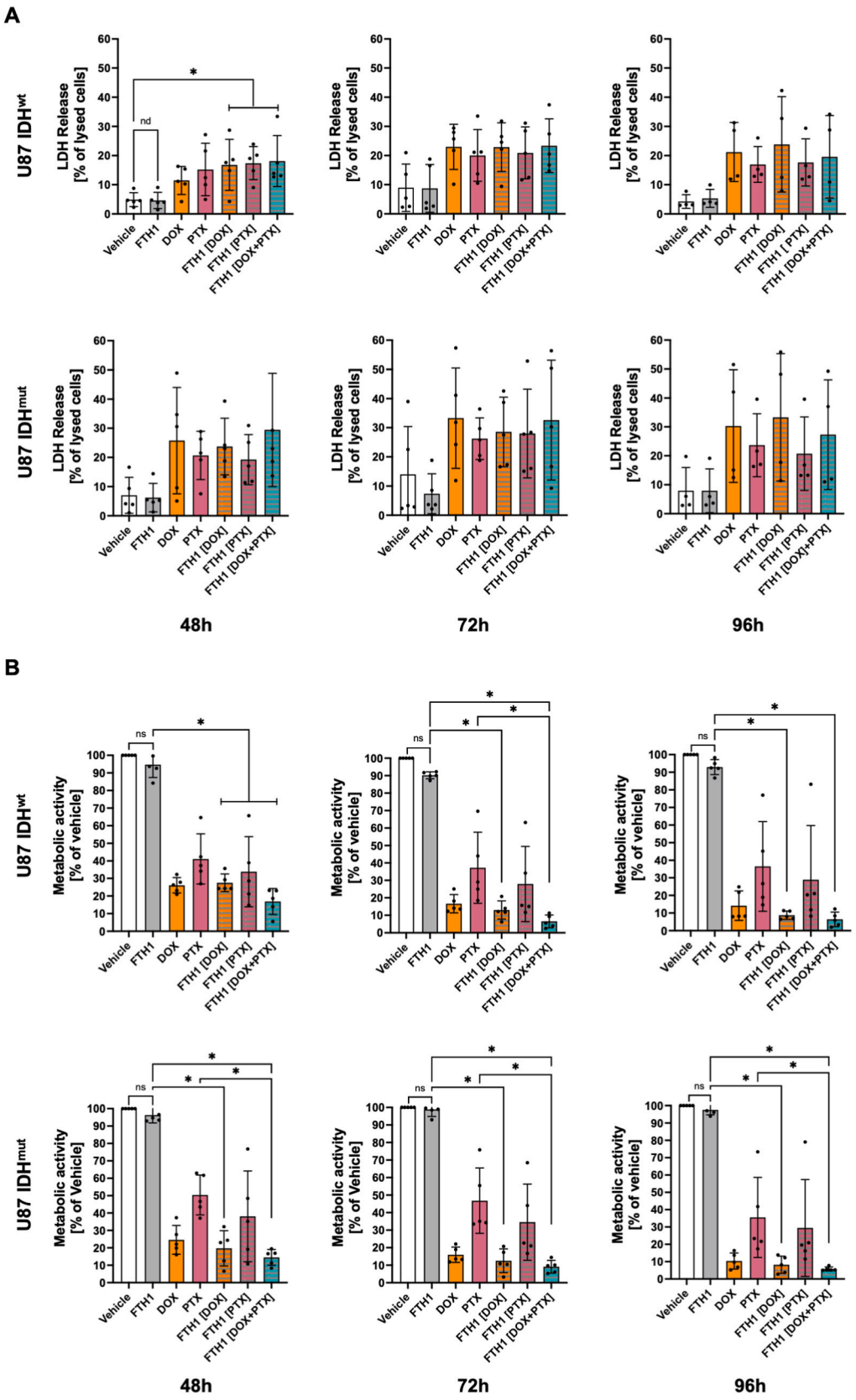
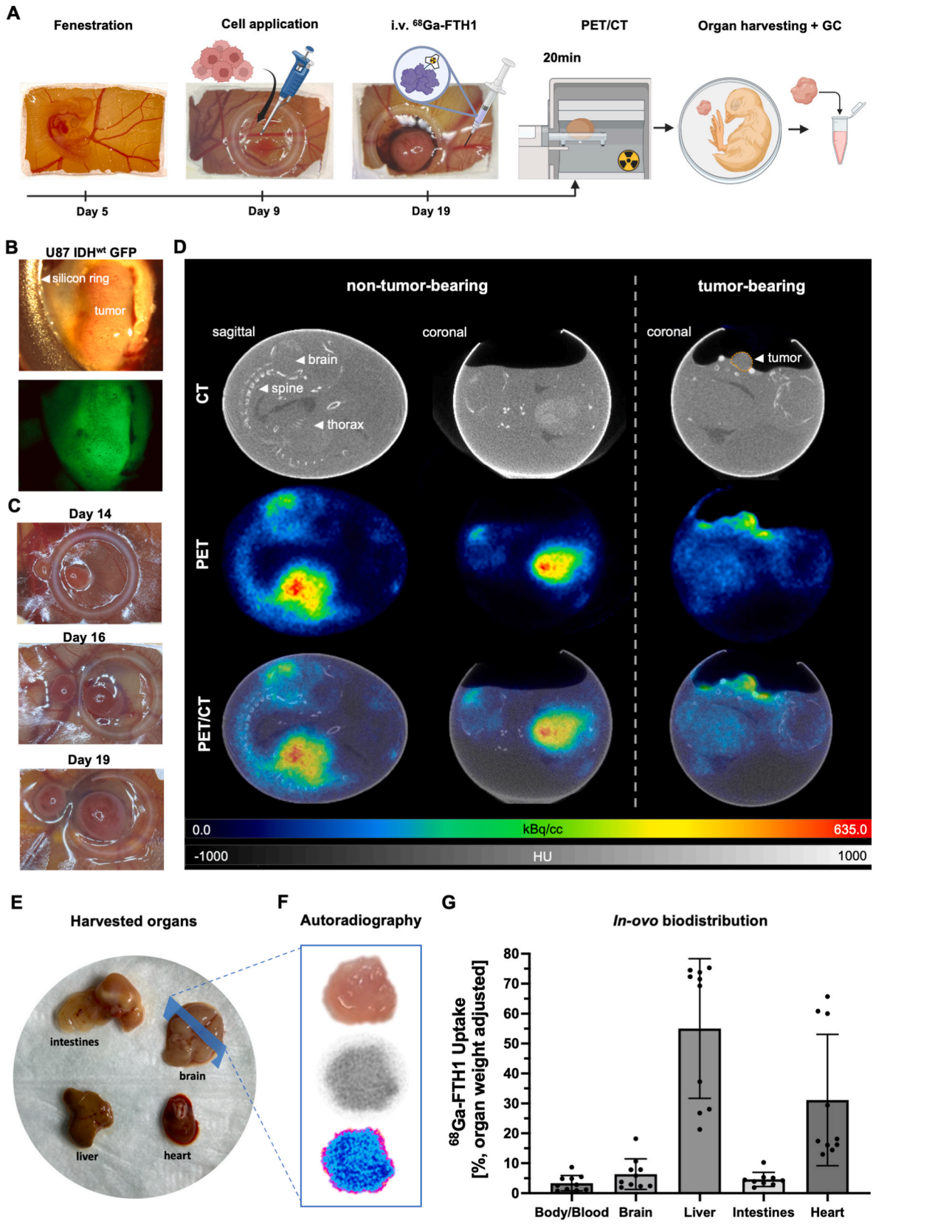


Fig. 3. Time-dependent assessment of cell viability and metabolic activity following treatment with FTH1 nanocarrier formulations in U87 glioma cells (**A**) CytoTox 96® Non-Radioactive Cytotoxicity Assay was performed, showing the LDH release in percentage of lysed cells, and (**B**) CellTiter-Blue® (CTB) Cell Viability Assay representing the cell viability relative to untreated cells after 48 h, 72 h, and 96 h in U87 IDH^{mut} or U87 IDH^{wt}. Bars are presented as means ± SD of 5 independent experiments with 3 technical replicates. A one-way ANOVA followed by a *Kruskal-Wallis test* was performed, *$p < 0.033$; **$p < 0.01$; ***$p < 0.001$; ns, not significant. (For interpretation of the references to color in this figure legend, the reader is referred to the Web version of this article.)



(caption on next page)

Fig. 4. Biodistribution and quantification of [54]Ga-FTH1 *in ovo* (A) Schematic illustration of the ectopic *in ovo* glioma model showing fenestration, tumor cell implantation (Day 9), intravenous (IV) injection of ^{68}Ga-FTH1 into the CAM vasculature (Day 19), PET/CT imaging (20 min post-injection), and organ harvesting. (**B**) Representative images of IDH^{wt} U87-GFP tumor under bright-field (top) and fluorescence (bottom) illumination. (**C**) Macroscopic views of the same ectopic tumor at different time points (Day 14, 16, 19). (**D**) CT, PET, and fused PET/CT images of chicken embryos (CEs) without (left/middle) and with (right) tumor after IV injection of ^{68}Ga-FTH1. Imaging was performed 20 min post-injection. Sagittal and coronal planes are shown for the healthy control group, and coronal for the tumor group. PET signal intensity ranges from 0.0 to 635.0 kBq/cc (blue to red). CT intensity ranges from -1000 to 1000 HU. (**E**) Representative image of harvested organs post-injection. (**F**) Autoradiography (ARG) of a brain section after IV injection with ^{68}Ga-FTH1 showing macroscopic tissue (top), radioactive signal (middle), and signal overlay (bottom). (**G**) *Ex vivo* quantification of ^{68}Ga-FTH1 uptake in dissected organs (body/blood, heart, liver, intestines, brain) by gamma counting (counts per minute), adjusted to organ weight and expressed as percentage of total recovered activity. Data are presented as mean ± SD (n = 9-10 animals). (For interpretation of the references to color in this figure legend, the reader is referred to the Web version of this article.)

exhibited a marked shift in treated IDH^{mut} tumors.

Phylogenetic mapping of differentially regulated kinases revealed broad suppression across several kinase families in IDH^{mut} tumors following treatment (Fig. 6C, left panel). In particular, kinomic inhibition was prominent in the AGC protein kinase family (PKA, PKG, PKC; e.g., AKT1-3, PRKCA/B), the CAMK family (e.g., CaMK2A/B, DAPK), and the CMGC family, including CDKs, MAPKs, GSK3, and CLKs (e.g., CDK1/2, MAPK9). These families regulate central survival, stress-response, and proliferation and cell-cycle pathways, consistent with reduced activity in signaling pathways associated with survival and proliferation (Fig. S4F and G). In contrast, treated IDH^{wt} tumors (right panel) exhibited widespread upregulation, particularly in Tyrosine kinases (TKs) and TK-like kinases (TKL; e.g., FGFRs, EGFR, PDGFRs), consistent with increased activation of growth factor-associated signaling pathways. Comparing the baseline kinase profiles of the IDH genotypes in untreated tumors, a suppression of some kinase families was detected, which showed an increase in this divergence after treatment (Fig. S4A and B).

Heatmaps of significantly modulated kinases corroborated these responses (Fig. 6D). IDH^{mut} tumors displayed extensive suppression of STKs and PTKs, whereas IDH^{wt} tumors showed strong PTK activation with comparatively limited STK modulation. Baseline kinase activity was broadly similar between genotypes, particularly within STKs, indicating that differences become more pronounced after treatment.

Pathway ORA confirmed these genotype-dependent adaptations (Fig. 6E–Table 1). GO analysis revealed an enrichment of pathways related to protein phosphorylation and higher activity in kinases and transferases (Fig. 6E). Additionally, immune response regulation was found to be upregulated. IDH^{mut} tumors showed reduced activity in kinases associated with PI3K-AKT, MAPK, and RTK signaling pathways, along with enhanced modulation of DNA-damage response, p53, and apoptotic signaling (Table 1). In contrast, IDH^{wt} tumors showed enrichment of growth-promoting cascades, including EGFR and Ras pathways, as well as immune-regulatory networks.

Together, these findings indicate that dual-drug FTH1 nanotherapy is associated with broad suppression of kinase families involved in survival and proliferation pathways in IDH^{mut} tumors, whereas IDH^{wt} tumors display increased activity of growth-associated kinase signaling pathways.

4. Discussion

Our study explored multifunctional, plant-derived FTH1 nanocages as a drug delivery and theranostic system for high-grade IDH-wildtype and -mutated gliomas. Using this platform, we sought to combine molecular imaging with the delivery of chemotherapeutics in experimental glioma tumor models characterized by distinct molecular backgrounds and therapy responses. By integrating drug encapsulation, pH-responsive release, and radiolabeling within a single nanoscale construct, we established a unified platform capable of both molecular imaging and drug delivery. Notably, our findings indicate differential therapeutic responses between tumors with distinct IDH status, highlighting the potential relevance of genotype-associated treatment effects in nanomedicine.

FTH1 nanocages exhibited robust radiometal chelation, consistently achieving > 95 % radiochemical yields with ^{68}Ga and retaining prolonged stability in HS (Fig. 1B–D). These features establish FTH1 as a robust scaffold for radiolabeling and molecular imaging. Drug loading experiments further demonstrated high encapsulation efficiency together with pH-dependent release of both DOX and PTX (Fig S1B, Fig. 1E–F), with enhanced drug release under acidic conditions. Such a release profile may be advantageous in gliomas, where the hypoxic tumor microenvironment is associated with extracellular acidification [55]. At the cellular level, FTH1 nanocages were internalized by both IDH^{wt} and IDH^{mut} U87 (Fig. 2D), with consistently higher uptake in IDH^{mut} cells. While both cell lines expressed the transferrin receptor CD71 (Fig. 2A), receptor expression alone does not explain this difference, suggesting that additional genotype-associated cellular properties may contribute to nanoparticle internalization. Competitive uptake experiments further support the involvement of TfR1 in FTH1 nanocage internalization (Fig. S2A). The partial inhibition observed following holotransferrin pre-incubation is consistent with previous reports indicating only partial competition between H-ferritin and holo-transferrin to TfR1 binding [56,57]. Electron microscopy confirmed endolysosomal localization and gradual degradation of FTH1 nanocages (Fig. 2C–E), comparable to previously reported intracellular processing of ferritin [58,59]. Functionally, drug-loaded nanocages induced a significant reduction in cell viability and metabolic activity, with dual-drug formulations (DOX + PTX) exerting the most potent effect (Fig. 3). These findings align with the complementary mechanisms of action of combined chemotherapeutic regimens, which can enhance the therapeutic outcomes [60,61]. Notably, bare ferritin nanocages showed negligible inherent toxicity, underscoring that the observed cell death was driven by the drug payload, rather than the carrier itself (Fig. 3). As LDH release and CellTiter Blue assess complementary aspects of the cellular responses, the partially divergent *in vitro* findings further support the use of multiple functional readouts to characterize treatment effects [62,63].

Additionally, our *in ovo* glioma studies displayed systemic biodistribution of ^{68}Ga-FTH1 with detectable intracerebral accumulation. PET/CT imaging corroborated cerebral uptake and focal tumor enrichment (Fig. 4D), while gamma counting and autoradiography confirmed broad brain parenchymal biodistribution (Fig. 4F and G). Although empty nanocages showed negligible intrinsic toxicity, the observed hepatic uptake (Fig. 4G) indicates the need for further evaluation of long-term clearance, since ferritin undergoes hepatic clearance and processing [64]. In the *in ovo* therapy setting, systemic administration of FTH1 [DOX + PTX] markedly reduced tumor growth rate and improved embryo survival (Fig. 5A and B). Serial imaging demonstrated that although both IDH genotypes responded to treatment, IDH^{mut} tumors exhibited a significantly pronounced therapeutic effect in growth kinetics, indicating higher sensitivity to the treatment (Fig. 5B). Gene expression analysis supported this, revealing increased Bax expression together with reduced IL-1β following treatment (Fig. 5D–F). In agreement with these molecular changes, increased TUNEL signal and cleaved Caspase-3 staining were observed in treated tumors, indicating activation of apoptotic pathways at the tissue level (Fig. 5F and Fig. S3D–F). Together with the kinomic data, these findings align with the clinical observation of enhanced chemosensitivity in IDH^{mut} gliomas and reinforce the potential of genotype-associated treatment responses in

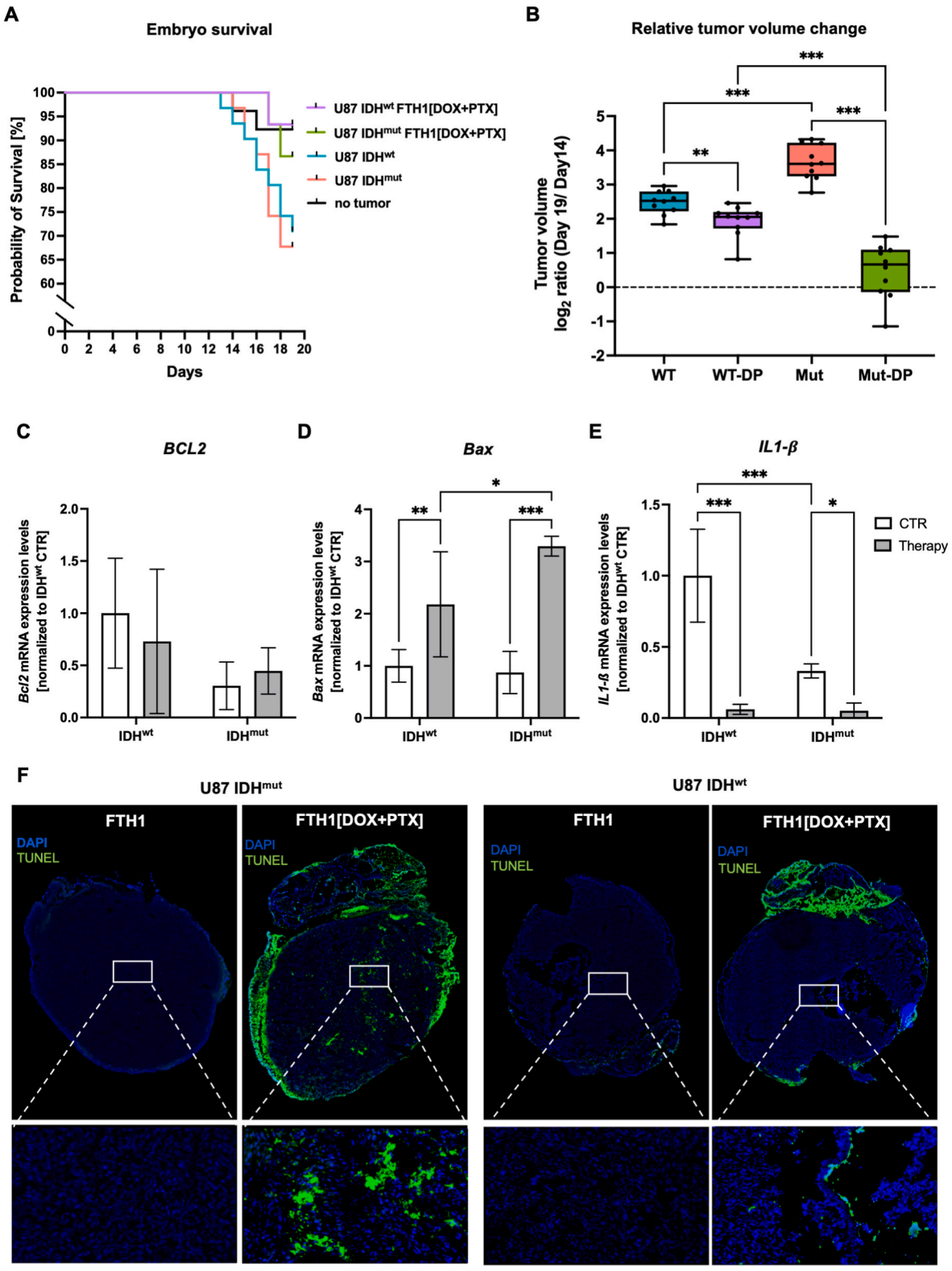
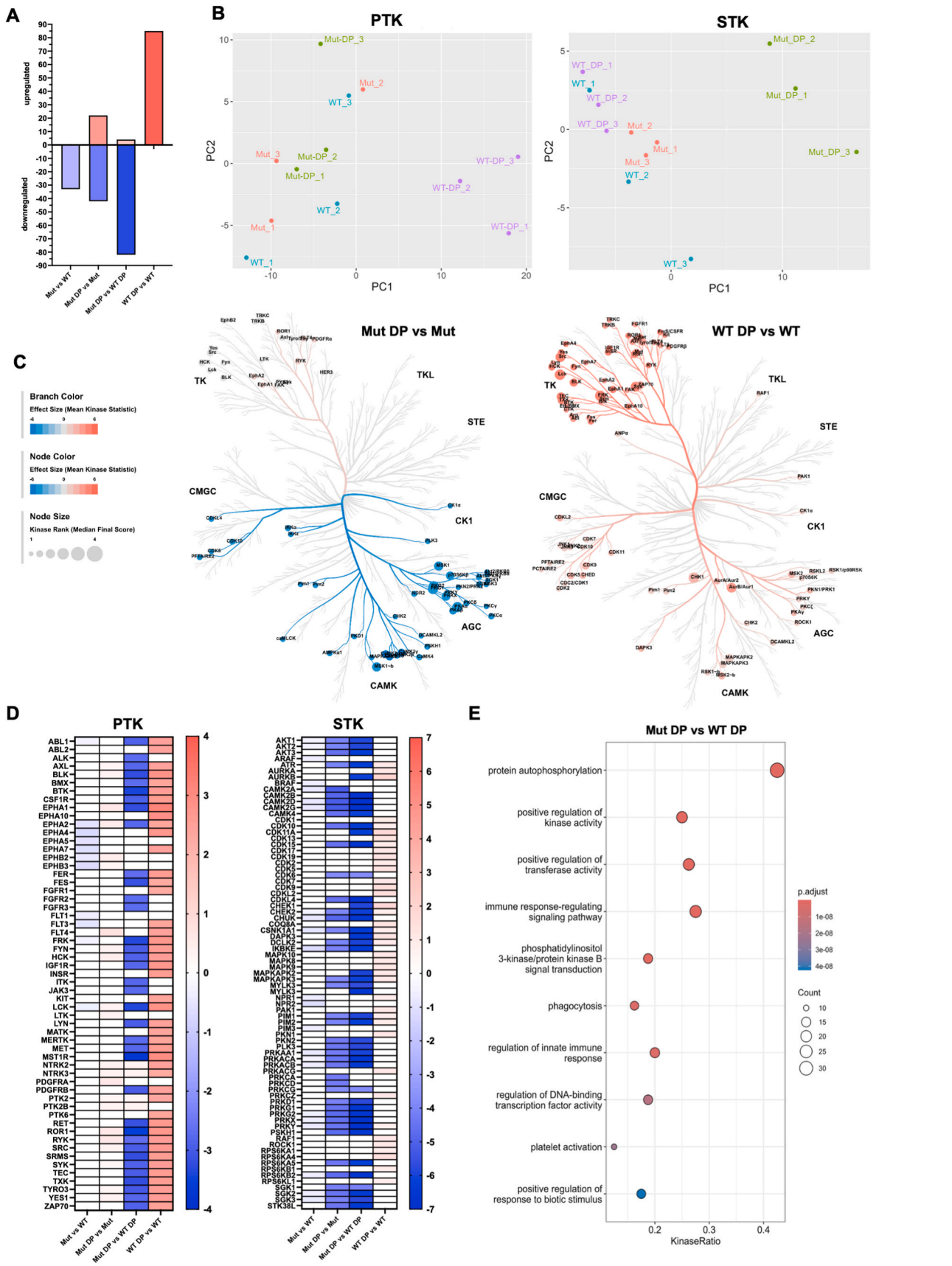


Fig. 5. Survival and tumor sizes of ectopic IDH^{mut} and IDH^{wt} tumors bearing chicken embryos (**A**) Kaplan-Meier survival analysis of CEs without tumor (n = 25), with untreated IDH^{wt} (n = 30) and IDH^{mut} (n = 30) tumors, and with corresponding treatment using FTH1[DOX + PTX] (n = 15). (**B**) CT-based relative change of tumor volume (ectopic U87 IDH^{wt} and U87 IDH^{mut}) between day 14 and 19. Embryos in the control group (n = 10) received vehicle (empty FTH1 nanocages, trypan blue and NaCl), while the treatment group received FTH1[DOX + PTX]. Boxplots show median and interquartile range, with whiskers indicating the minimum and maximum values of the individual log2 fold change in tumor volume (day 19/day 14) (n = 10). An unpaired *t*-test was performed, *p < 0.033; **p < 0.01; ***p < 0.001; ns, not significant. (**C-E**) qPCR analysis of Bcl2, BAX, and IL1-β expression in FTH1 [DOX + PTX]-treated or control ectopic tumors. mRNA expression levels are shown normalized to IDH^{wt} CTR. Bars represent mean ± SD of 6 technical replicates (n = 9 tumors). *p < 0.033; **p < 0.01; ***p < 0.001; ns, not significant. (**F**) Representative TUNEL staining of U87 IDH^{wt} and U87 IDH^{mut} tumors following treatment with FTH1 or FTH1[DOX + PTX]. Green: TUNEL-positive cells; blue: DAPI. (For interpretation of the references to color in this figure legend, the reader is referred to the Web version of this article.)



(caption on next page)

Fig. 6. Kinase activity profiling of STK and PTK in ectopic U87 IDH^{wt} and IDH^{mut} after FTH1 [DOX + PTX] treatment using the PamStation®12 platform. Kinase profiling was performed on tumor lysates derived from control group U87 IDH^{wt} (WT), control group U87 IDH^{mut} (Mut), and their corresponding FTH1[DOX + PTX] counterparts (WT DP or Mut DP, respectively). Each biological replicate consists of 3-4 pooled tumor specimens (a total of n = 12-14 individual tumors per condition) (**A**) Absolute numbers of significantly upregulated and downregulated kinases are shown for four key comparisons (Mut vs WT, Mut DP vs Mut, Mut DP vs WT DP, WT DP vs WT). (**B**) PCA for PTKs (left) and STKs (right). Each dot represents an individual pooled sample. PC1 and PC2 capture the major axes of variance in the data set. (**C**) Combined STK and PTK kinomic tree visualizations (Coral Tree) for comparisons: Mut DP vs Mut (left) and WT DP vs WT (right). Kinases are mapped onto a phylogenetic tree of the human protein kinase family. Node size corresponds to kinase rank (median final score), node and branch color denote the effective size (mean kinase statistic, blue: downregulated, red: upregulated). (**D**) Heatmaps of the significantly differentially active kinases across the four key comparisons. Red color reflects increased activity (based on mean kinase statistic), while blue color reflects decreased activity, consistent with reduced phosphorylation of the peptides. (**E**) Dot plot for overrepresentation analysis (ORA), analyzed with Gene Ontology (GO), indicating the extent and significance of pathways regulated in Mut DP versus WT DP. Results are ranked according to kinase ratio, and dot size represents the number/counts of involved kinases. Color indicates adjusted p-values, and the x-axis displays the kinase ratio. (For interpretation of the references to color in this figure legend, the reader is referred to the Web version of this article.)

Table 1
Pathway enrichment analysis of differentially regulated kinases in treated IDH^{mut} tumors. Significantly enriched pathways (adjusted p-values shown) classified into DNA-damage/cell-death, immune–inflammatory signaling, glioma-associated pathways, and tumor growth/proliferation signaling.

Description	ID	Adjusted *P*-value
DNA-Damage and Cell Death		
DNA damage response	WP707	1.30E-03
ATM signaling in development and disease	WP3878	1.99E-05
DNA IR-double strand breaks and cellular response *via* ATM	WP3959	4.36E-03
ATM signaling pathway	WP2516	1.32E-02
PD-L1 expression and PD-1 checkpoint pathway in cancer	hsa05235	2.94E-07
Cellular senescence	hsa04218	9.52E-05
p53 signaling pathway	hsa04115	3.03E-02
Apoptosis	hsa04210	3.24E-02
Immune and Inflammatory signaling		
IL-3 signaling pathway	WP286	3,01E-06
IL-2 signaling pathway	WP49	1,41E-05
IL-5 signaling pathway	WP127	1.61E-04
IL-4 signaling pathway	WP395	4.17E-03
IL-7 signaling pathway	WP205	4.37E-03
IL-1 signaling pathway	WP195	2.72E-02
TLR4 signaling and tolerance	WP3851	4.89E-02
B cell receptor signaling pathway	WP23	2.16E-07
T cell receptor and co-stimulatory signaling	WP2583	2.00E-06
Chemokine signaling pathway	WP3929	1.39E-05
Interferon type I signaling pathways	WP585	5.04E-04
Neuroinflammation	WP4919	1.46E-02
Chemokine signaling pathway	hsa04062	2.03E-06
T cell receptor signaling pathway	hsa04660	2.60E-06
Inflammatory mediator regulation of TRP channels	hsa04750	4.28E-05
TNF signaling pathway	hsa04668	4.32E-03
Glioma associated		
Brain-derived neurotrophic factor (BDNF) signaling pathway	WP2380	3.07E-05
Glioma	hsa05214	6.25E-10
Neurotrophin signaling pathway	hsa04722	3.22E-08
Tumor Signaling and Proliferation		
Ras signaling	WP4223	1.99E-09
Focal adhesion: PI3K-Akt-mTOR-signaling pathway	WP3932	3.01E-06
VEGFA-VEGFR2 signaling pathway	WP3888	1.17E-03
EGF/EGFR signaling pathway	WP437	8.35E-03
Relationship between inflammation, COX-2 and EGFR	WP4483	3.35E-04
PI3K-Akt signaling pathway	hsa04151	4.71E-11
EGFR tyrosine kinase inhibitor resistance	hsa01521	8.66E-11
MAPK signaling pathway	a04010	3.32E-09

nanotherapies [65,66]. Kinomic profiling provided a functional overview of treatment-associated changes in kinase signaling of treated and untreated tumors. Dual-drug nanotherapy induced divergent kinase responses according to the tumor IDH-mutation status. Treatment led to a broad suppression of AGC- and CMGC-family kinases in IDH^{mut} gliomas (Fig. 6C), which are pivotal regulators of survival, proliferation, and cell cycle progression [67,68]. The global silencing of pro-survival pathways aligns with the observed decrease in tumor growth (Table 1, Fig. S4D). By contrast, IDH^{wt} tumors exhibited a compensatory upregulation of receptor tyrosine kinases and Ras-associated cascades, sustaining proliferation potential despite cytotoxic pressure (Fig. 6C, Fig. S4E). Correlating with the pronounced tumor growth suppression observed in IDH^{mut} tumors, these findings provide functional signaling context for stratifying nanotherapy responses and molecular diagnostic potential, providing further insight into personalized therapy regimens.

Current therapeutic options for high-grade gliomas remain limited, with a poor prognostic outlook under the current standard of care [1,2]. Even IDH^{mut} grade IV astrocytomas, despite having a better prognosis, display resistance to conventional regimens [7,8]. These challenges call for novel delivery systems and personalized therapeutic strategies [14]. Ferritin nanocages represent a promising solution, exploiting transferrin receptor-mediated transcytosis to cross the BBB and enable drug encapsulation while retaining structural stability [40,41,54]. Moreover, the use of plant-derived FTH1 within the *in ovo* glioma model mitigates the cost and scalability barriers often encountered with recombinant mammalian systems [42]. Building on this technical advantage, our study demonstrates the efficient loading of DOX and PTX, two established cytostatics for GBM models, which are unable to penetrate the BBB in their molecular form [28–30,69]. This dose-reduction strategy was chosen to limit potential systemic toxicity while enabling combined exposure to two mechanistically distinct cytotoxic agents. Although the combined DOX/PTX treatment produced a greater therapeutic effect than the corresponding single-drug treatments, the pharmacological interaction between both agents remains to be defined, as it may vary depending on the applied drug ratio. Future studies should therefore systematically evaluate different DOX:PTX ratios to identify the optimal therapeutic combination for this nanoplatform. Nevertheless, these findings support further investigation of combined nanoparticle-based delivery of mechanistically distinct chemotherapeutic agents for high-grade glioma treatment.

Our radiolabeling with ^{68}Ga *via* NOTA proved efficient and stable, consistent with established PET approaches for protein-based nanocarriers [70]. These properties support the potential of ferritin nanocages for future theranostic applications with different isotopes such as lutetium-177 [71,72]. Besides *in vitro* therapy studies, we employed the CAM model, which has gained recognition as an economical and scalable alternative to rodent systems for evaluating tumor targeting and biodistribution in preclinical research, to explore the translational potential of FTH1 [73]. By adapting this model for high-grade gliomas, we demonstrate its value as a high-throughput platform for evaluating nanocarriers. Importantly, the CAM system recapitulates key aspects of vascularization and tumor progression in the relevant environment, simultaneously enabling imaging and tissue analyses of genotype-dependent therapeutic responses. While the chicken embryo BBB does not fully recapitulate the mammalian counterpart, this model can still capture relevant aspects of high-grade gliomas, where barrier integrity is often compromised [74,75]. Additionally, this model lacks an immune compartment, and its limited developmental window precludes the assessment of long-term therapeutic efficacy and survival outcomes. Despite these limitations, we were able to demonstrate a therapeutic effect on tumor growth and survival within the experimental

Table 2
List of qPCR primers.

Gene	Forward	Reverse	AT [°C]	Species
BCL-2	AGGATGGGATGCCTTTGTGG	AGAGTGATGCAAGCTCCCAC	58.8	chicken
CASP1	CCTCATAGACACCGTACGCC	TGAGCACACAGTCTCAGCTG	58.3	chicken
BAK1	CATGGACCCGGAGATCATGG	CTTGTTGATGTCGTCCCCGA	60.0	chicken
GAPDH	ACTGTCAAGGCTGAGAACGG	GCCTTCTCCATGGTGGTGAA	59.2	chicken
GAPDH	CCTGCACCACCAACTGCTTA	GGCCATCCACAGTCTTCTCAG	59.3	human
L-1ß	CTTCGAGGCACAAGGCACAA	TTCACTGGCGAGCTCAGGTA	59.8	human
BAX	CATGAAGACAGGGGCCCTTT	CTTCTTGGTGGACGCATCCT	59.4	human
BCL-2	GAACTGGGGGAGGATTGTGG	ACCTACCCAGCCTCCGTTAT	59.3	human

time frame. Nevertheless, several aspects should be considered when interpreting the results. The use of an isogenic U87-based model allows controlled comparison of IDH status but does not fully capture the biological heterogeneity of patient-derived gliomas. In addition, while the CAM system enables rapid *in vivo* screening of biodistribution and therapeutic effects, it cannot fully reproduce the structural and physiological characteristics of the mammalian blood–brain barrier. Future studies in mammalian models and patient-derived systems will therefore be required to further validate the translational potential of this nanoplatform and assess long-term therapeutic efficiency.

A strength of this study lies in the use of kinomic profiling to systematically capture therapy-induced divergence in signaling activity, as it interrogates the functional state of kinase networks [45,76]. This enables a functional view of how intracellular signaling networks adapt to treatment and thus provides a mechanistic framework that goes beyond descriptive observations. In the context of gliomas, with their redundant signaling cascades and adaptive resistance, this provides a tool to capture the complexity of therapeutic responses. Our data reveal IDH-status-associated signaling differences, highlighting the importance of IDH mutational status in therapy susceptibility in glioma. The vulnerability and sensitivity of IDH^{mut} tumors compared to IDH^{wt} counterparts were already observed in previous reports [77–79]. Importantly, our kinomic profiling confirms these findings and provides a mechanistic readout to clinical observations. Moreover, this analysis offers the potential to move toward individualized treatments by matching kinase level signatures with targeted interventions. These findings may be particularly relevant for patients with IDH^{mut} grade IV astrocytomas, who generally display prolonged survival but retain a high risk of therapeutic resistance [7,8]. Such insights may guide the development of rational combination therapies, leveraging pathway vulnerabilities in IDH^{mut} grade IV astrocytomas. Tailoring nanotherapies to specific IDH profiles could complement existing treatment regimens and address unmet clinical needs.

5. Conclusion

In conclusion, this study establishes ferritin nanocages as a multifunctional platform for theranostic drug delivery in glioma models. The nanocages demonstrated efficient radiolabeling, dual-drug loading, and pH-responsive release, together with robust cellular uptake and measurable intracerebral distribution in the CAM model. Kinomic profiling revealed differential kinase signaling responses between tumors with different IDH status following therapy. While further validation in mammalian models will be required, these findings highlight the potential of ferritin nanocages as a platform for image-guided drug delivery and for exploring genotype-associated differences in therapeutic response in high-grade glioma models.

Ethics approval and consent to participate

Not applicable.

Consent for publication

Not applicable.

Availability of data and materials

All data supporting the findings of this study are available within the article and its supplementary information files. Raw data and additional information related to this paper may be requested from the corresponding author upon reasonable request.

Funding

This work was funded by an internal grant (START grant 111/17, PH) and the German Research Foundation (DFG), HA 9566/1–1 (PH) and supported by the “Clinician Scientist program” of the Faculty of Medicine, RWTH Aachen University (PH). The funding body did not influence the design of the study, data acquisition or on analyses and interpretation of data.

CRediT authorship contribution statement

Mara Schietinger: Data curation, Formal analysis, Investigation, Methodology, Visualization, Writing – original draft. **Sabri E.M. Sahnoun:** Investigation, Methodology, Validation, Writing – review & editing. **Edda J. Krug:** Investigation, Visualization, Writing – review & editing. **Philipp N. Loewe:** Investigation, Visualization, Writing – review & editing. **Paolo Alimonti:** Investigation, Visualization, Writing – review & editing. **Emiel P.C. van der Vorst:** Investigation, Visualization, Writing – review & editing. **Najaf Mammadbayli:** Investigation, Writing – review & editing. **Agnieszka Morgenroth:** Writing – review & editing. **Daniel Müller:** Resources, Writing – review & editing. **Eva M. Buhl:** Investigation, Visualization, Writing – review & editing. **Alaa A. Gad:** Investigation, Visualization, Writing – review & editing. **Bernd Neumaier:** Methodology, Writing – review & editing. **Felix M. Mottaghy:** Resources, Writing – review & editing. **Jörg B. Schulz:** Resources, Writing – review & editing. **Katherine A. Vallis:** Conceptualization, Writing – review & editing. **Pardes Habib:** Conceptualization, Data curation, Formal analysis, Methodology, Project administration, Resources, Supervision, Visualization, Writing – review & editing.

Declaration of competing interest

The authors declare that they have no known competing financial interests or personal relationships that could have appeared to influence the work reported in this paper.

Acknowledgements

We thank Laura Wend, Aaron Fehr, and Carina Stegmayr for their excellent technical assistance.

Appendix A. Supplementary data

Supplementary data to this article can be found online at https://doi.org/10.1016/j.mtbio.2026.103539.

Data availability

Data will be made available on request.

References

[1] J. van Dijck, et al., Survival prediction in glioblastoma: 10-year follow-up from the Dutch neurosurgery quality registry, J. Neuro Oncol. 174 (2025) 753–764, https://doi.org/10.1007/s11060-025-05080-3.

[2] D. Sipos, et al., Glioblastoma: clinical presentation, multidisciplinary management, and long-term outcomes, Cancers (Basel) 17 (2025), https://doi.org/10.3390/cancers17010146.

[3] S. Grochans, et al., Epidemiology of glioblastoma multiforme-literature review, Cancers (Basel) 14 (2022), https://doi.org/10.3390/cancers14102412.

[4] A. Olar, K.D. Aldape, Using the molecular classification of glioblastoma to inform personalized treatment, J. Pathol. 232 (2014) 165–177, https://doi.org/10.1002/path.4282.

[5] D.N. Louis, et al., The 2016 World Health organization classification of tumors of the central nervous system: a summary, Acta Neuropathol. 131 (2016) 803–820, https://doi.org/10.1007/s00401-016-1545-1.

[6] H. Yan, et al., IDH1 and IDH2 mutations in gliomas, N. Engl. J. Med. 360 (2009) 765–773, https://doi.org/10.1056/NEJMoa0808710.

[7] S. Han, et al., IDH mutation in glioma: molecular mechanisms and potential therapeutic targets, Br. J. Cancer 122 (2020) 1580–1589, https://doi.org/10.1038/s41416-020-0814-x.

[8] R. Alshiekh Nasany, M.I. de la Fuente, Therapies for IDH-mutant gliomas, Curr. Neurol. Neurosci. Rep. 23 (2023) 225–233, https://doi.org/10.1007/s11910-023-01265-3.

[9] A. Ou, W.K.A. Yung, N. Majd, Molecular mechanisms of treatment resistance in glioblastoma, Int. J. Mol. Sci. 22 (2020), https://doi.org/10.3390/ijms22010351.

[10] F. Mo, A. Pellerino, R. Soffietti, R. Rudà, Blood-Brain barrier in brain tumors: biology and clinical relevance, Int. J. Mol. Sci. 22 (2021), https://doi.org/10.3390/ijms222312654.

[11] J.F. Deeken, W. Löscher, The blood-brain barrier and cancer: transporters, treatment, and Trojan horses, Clin. Cancer Res. 13 (2007) 1663–1674, https://doi.org/10.1158/1078-0432.Ccr-06-2854.

[12] C. Neftel, et al., An integrative model of cellular states, plasticity, and genetics for glioblastoma, Cell 178 (2019) 835–849.e821, https://doi.org/10.1016/j.cell.2019.06.024.

[13] H. Ghaznavi, et al., New insights into targeted therapy of glioblastoma using smart nanoparticles, Cancer Cell Int. 24 (2024) 160, https://doi.org/10.1186/s12935-024-03331-3.

[14] M. Duan, et al., Blood-brain barrier conquest in glioblastoma nanomedicine: strategies, clinical advances, and emerging challenges, Cancers (Basel) 16 (2024), https://doi.org/10.3390/cancers16193300.

[15] Y. Zeng, et al., Aptamer-functionalized nanoplatforms overcoming temozolomide resistance in synergistic chemo/photothermal therapy through alleviating tumor hypoxia, Nano Res. 16 (2023) 9859–9872, https://doi.org/10.1007/s12274-023-5742-7.

[16] N.J. Abbott, L. Rönnbäck, E. Hansson, Astrocyte-endothelial interactions at the blood-brain barrier, Nat. Rev. Neurosci. 7 (2006) 41–53, https://doi.org/10.1038/nrn1824.

[17] B. Obermeier, R. Daneman, R.M. Ransohoff, Development, maintenance and disruption of the blood-brain barrier, Nat Med 19 (2013) 1584–1596, https://doi.org/10.1038/nm.3407.

[18] R. Daneman, A. Prat, The blood-brain barrier, Cold Spring Harb Perspect Biol 7 (2015) a020412, https://doi.org/10.1101/cshperspect.a020412.

[19] W.M. Pardridge, Drug transport across the blood-brain barrier, J. Cereb. Blood Flow Metab. 32 (2012) 1959–1972, https://doi.org/10.1038/jcbfm.2012.126.

[20] R. Pandit, L. Chen, J. Götz, The blood-brain barrier: physiology and strategies for drug delivery, Adv. Drug Deliv. Rev. 165-166 (2020) 1–14, https://doi.org/10.1016/j.addr.2019.11.009.

[21] W.M. Pardridge, The blood-brain barrier: bottleneck in brain drug development, NeuroRx 2 (2005) 3–14, https://doi.org/10.1602/neurorx.2.1.3.

[22] W.A. Banks, From blood-brain barrier to blood-brain interface: new opportunities for CNS drug delivery, Nat. Rev. Drug Discov. 15 (2016) 275–292, https://doi.org/10.1038/nrd.2015.21.

[23] P. Yang, et al., IDH mutation and MGMT promoter methylation in glioblastoma: results of a prospective registry, Oncotarget 6 (2015) 40896–40906, https://doi.org/10.18632/oncotarget.5683.

[24] N. Singh, A. Miner, L. Hennis, S. Mittal, Mechanisms of temozolomide resistance in glioblastoma - a comprehensive review, Cancer Drug Resist 4 (2021) 17–43, https://doi.org/10.20517/cdr.2020.79.

[25] C.F. Thorn, et al., Doxorubicin pathways: pharmacodynamics and adverse effects, Pharmacogenet. Genom. 21 (2011) 440–446, https://doi.org/10.1097/FPC.0b013e32833ffb56.

[26] E.K. Rowinsky, R.C. Donehower, Paclitaxel (Taxol), N. Engl. J. Med. 332 (1995) 1004–1014, https://doi.org/10.1056/nejm199504133321507.

[27] I. Sardi, et al., Delivery of doxorubicin across the blood-brain barrier by ondansetron pretreatment: a study in vitro and in vivo, Cancer Lett. 353 (2014) 242–247, https://doi.org/10.1016/j.canlet.2014.07.018.

[28] S. Fellner, et al., Transport of paclitaxel (taxol) across the blood-brain barrier in vitro and in vivo, J. Clin. Investig. 110 (2002) 1309–1318, https://doi.org/10.1172/jci15451.

[29] V.A. Arrieta, et al., Ultrasound-mediated delivery of doxorubicin to the brain results in immune modulation and improved responses to PD-1 blockade in gliomas, Nat. Commun. 15 (2024) 4698, https://doi.org/10.1038/s41467-024-48326-w.

[30] S. Pacioni, et al., Mesenchymal stromal cells loaded with paclitaxel induce cytotoxic damage in glioblastoma brain xenografts, Stem Cell Res. Ther. 6 (2015) 194, https://doi.org/10.1186/s13287-015-0185-z.

[31] L. Wang, et al., Analysis of the cytotoxic effects, cellular uptake and cellular distribution of paclitaxel-loaded nanoparticles in glioblastoma cells in vitro, Exp. Ther. Med. 21 (2021) 292, https://doi.org/10.3892/etm.2021.9723.

[32] M. Norouzi, et al., Doxorubicin-loaded iron oxide nanoparticles for glioblastoma therapy: a combinational approach for enhanced delivery of nanoparticles, Sci. Rep. 10 (2020) 11292, https://doi.org/10.1038/s41598-020-68017-y.

[33] M. Aryal, C.D. Arvanitis, P.M. Alexander, N. McDannold, Ultrasound-mediated blood-brain barrier disruption for targeted drug delivery in the central nervous system, Adv. Drug Deliv. Rev. 72 (2014) 94–109, https://doi.org/10.1016/j.addr.2014.01.008.

[34] F. Danhier, O. Feron, V. Préat, To exploit the tumor microenvironment: passive and active tumor targeting of nanocarriers for anti-cancer drug delivery, J. Contr. Release 148 (2010) 135–146, https://doi.org/10.1016/j.jconrel.2010.08.027.

[35] X. Sun, Y. Hong, Y. Gong, S. Zheng, D. Xie, Bioengineered ferritin nanocarriers for cancer therapy, Int. J. Mol. Sci. 22 (2021), https://doi.org/10.3390/ijms22137023.

[36] J. He, K. Fan, X. Yan, Ferritin drug carrier (FDC) for tumor targeting therapy, J. Contr. Release 311-312 (2019) 288–300, https://doi.org/10.1016/j.jconrel.2019.09.002.

[37] K.B. Johnsen, et al., Targeting transferrin receptors at the blood-brain barrier improves the uptake of immunoliposomes and subsequent cargo transport into the brain parenchyma, Sci. Rep. 7 (2017) 10396, https://doi.org/10.1038/s41598-017-11220-1.

[38] A.M. Rosager, et al., Transferrin receptor-1 and ferritin heavy and light chains in astrocytic brain tumors: expression and prognostic value, PLoS One 12 (2017) e0182954, https://doi.org/10.1371/journal.pone.0182954.

[39] M.J. Ramalho, J.A. Loureiro, M.A.N. Coelho, M.C. Pereira, Transferrin receptor-targeted nanocarriers: overcoming barriers to treat glioblastoma, Pharmaceutics 14 (2022), https://doi.org/10.3390/pharmaceutics14020279.

[40] W. Liu, et al., Target delivering paclitaxel by ferritin heavy chain nanocages for glioma treatment, J. Contr. Release 323 (2020) 191–202, https://doi.org/10.1016/j.jconrel.2019.12.010.

[41] K. Fan, et al., Ferritin nanocarrier traverses the blood brain barrier and kills glioma, ACS Nano 12 (2018) 4105–4115, https://doi.org/10.1021/acsnano.7b06969.

[42] M. Knodler, et al., Simple plant-based production and purification of the assembled human ferritin heavy chain as a nanocarrier for tumor-targeted drug delivery and bioimaging in cancer therapy, Biotechnol. Bioeng. 120 (2023) 1038–1054, https://doi.org/10.1002/bit.28312.

[43] Y. Lu, et al., Chemosensitivity of IDH1-Mutated gliomas due to an impairment in PARP1-Mediated DNA repair, Cancer Res. 77 (2017) 1709–1718, https://doi.org/10.1158/0008-5472.Can-16-2773.

[44] M.P. Peppelenbosch, Kinome profiling, Sci. Tech. Rep. 2012 (2012) 306798, https://doi.org/10.6064/2012/306798.

[45] F. Fabro, et al., Novel kinome profiling technology reveals drug treatment is patient and 2D/3D model dependent in glioblastoma, Front. Oncol. 12 (2022) 1012236, https://doi.org/10.3389/fonc.2022.1012236.

[46] A.M. Jermakowicz, et al., RAPID resistance to BET inhibitors is mediated by FGFR1 in glioblastoma, Sci. Rep. 14 (2024) 9284, https://doi.org/10.1038/s41598-024-60031-8.

[47] M. Hagedorn, et al., Accessing key steps of human tumor progression in vivo by using an avian embryo model, Proc. Natl. Acad. Sci. U. S. A. 102 (2005) 1643–1648, https://doi.org/10.1073/pnas.0408622102.

[48] Y. Liu, et al., Functional paclitaxel-manganese-doped mesoporous silica nanoparticles for orthotopic brain glioma targeted therapy, Mater. Des. 238 (2024) 112715, https://doi.org/10.1016/j.matdes.2024.112715.

[49] A. Nangsuay, et al., Effects of breeder age, broiler strain, and eggshell temperature on development and physiological status of embryos and hatchlings, Poult. Sci. 95 (2016) 1666–1679, https://doi.org/10.3382/ps/pew080.

[50] T. Zeyen, et al., Microglial-specific depletion of TAK1 is neuroprotective in the acute phase after ischemic stroke, Journal of Molecular Medicine 98 (2020) 833–847, https://doi.org/10.1007/s00109-020-01916-9.

[51] A. Bonnin-Marquez, S.L. Maas, M. Corcini-Berndt, E.P.C. Van der Vorst, Unbiased kinome profiling identifies key and novel mediators of chronic kidney disease in hyperlipidemic mice, Front. Physiol. 16 (2025) 1684982, https://doi.org/10.3389/fphys.2025.1684982.

[52] C.S. Chirumamilla, et al., Profiling activity of cellular kinases in migrating T-Cells, Methods Mol. Biol. 99-113 (2019), https://doi.org/10.1007/978-1-4939-9036-8_13, 1930.

[53] G. Yu, L.G. Wang, Y. Han, Q.Y. He, clusterProfiler: an R package for comparing biological themes among gene clusters, OMICS 16 (2012) 284–287, https://doi.org/10.1089/omi.2011.0118.

[54] M. Khoshnejad, H. Parhiz, V.V. Shuvaev, I.J. Dmochowski, V.R. Muzykantov, Ferritin-based drug delivery systems: hybrid nanocarriers for vascular immunotargeting, J. Contr. Release 282 (2018) 13–24, https://doi.org/10.1016/j.jconrel.2018.02.042.
[55] N.H. Boyd, et al., Glioma stem cells and their roles within the hypoxic tumor microenvironment, Theranostics 11 (2021) 665–683, https://doi.org/10.7150/thno.41692.
[56] L. Li, et al., Binding and uptake of H-ferritin are mediated by human transferrin receptor-1, Proc. Natl. Acad. Sci. U. S. A. 107 (2010) 3505–3510, https://doi.org/10.1073/pnas.0913192107.
[57] L.C. Montemiglio, et al., Cryo-EM structure of the human ferritin-transferrin receptor 1 complex, Nat. Commun. 10 (2019) 1121, https://doi.org/10.1038/s41467-019-09098-w.
[58] S. Ravishankar, et al., Protein nanoparticle cellular fate and responses in murine macrophages, NPG Asia Mater. 15 (2023) 1, https://doi.org/10.1038/s41427-022-00453-w.
[59] T. Ohshima, H. Yamamoto, Y. Sakamaki, C. Saito, N. Mizushima, NCOA4 drives ferritin phase separation to facilitate macroferritinophagy and microferritinophagy, J. Cell Biol. 221 (2022), https://doi.org/10.1083/jcb.202203102.
[60] H.H. Duong, L.Y. Yung, Synergistic co-delivery of doxorubicin and paclitaxel using multi-functional micelles for cancer treatment, Int J Pharm 454 (2013) 486–495, https://doi.org/10.1016/j.ijpharm.2013.06.017.
[61] Y. Wang, et al., Lung cancer combination therapy: co-delivery of paclitaxel and doxorubicin by nanostructured lipid carriers for synergistic effect, Drug Deliv. 23 (2016) 1398–1403, https://doi.org/10.3109/10717544.2015.1055619.
[62] J. O'Brien, I. Wilson, T. Orton, F. Pognan, Investigation of the alamar blue (Resazurin) fluorescent dye for the assessment of mammalian cell cytotoxicity, Eur. J. Biochem. 267 (2000) 5421–5426, https://doi.org/10.1046/j.1432-1327.2000.01606.x.
[63] T. Decker, M.L. Lohmann-Matthes, A quick and simple method for the quantitation of lactate dehydrogenase release in measurements of cellular cytotoxicity and tumor necrosis factor (TNF) activity, J. Immunol. Methods 115 (1988) 61–69, https://doi.org/10.1016/0022-1759(88)90310-9.
[64] A. Macone, et al., Challenges in exploiting human H ferritin nanoparticles for drug delivery: navigating physiological constraints, Wiley Interdiscip. Rev. Nanomed. Nanobiotechnol. 16 (2024) e2016, https://doi.org/10.1002/wnan.2016.
[65] L. Lin, et al., Mutant IDH1 enhances temozolomide sensitivity via regulation of the ATM/CHK2 pathway in Glioma, Cancer Res. Treat. 53 (2021) 367–377, https://doi.org/10.4143/crt.2020.506.
[66] T. Lanman, I. Densmore, S. Nagpal, L. Recht, T. McGranahan, Characteristics and outcomes of patients with IDH-Mutant grade 2 and 3 gliomas after deferred or adjuvant radiotherapy, Neurology 105 (2025) e213797, https://doi.org/10.1212/wnl.0000000000213797.
[67] I. Chowdhury, G. Dashi, S. Keskitalo, CMGC kinases in health and cancer, Cancers (Basel) 15 (2023), https://doi.org/10.3390/cancers15153838.
[68] A.E. Leroux, J.O. Schulze, R.M. Biondi, AGC kinases, mechanisms of regulation and innovative drug development, Semin. Cancer Biol. 48 (2018) 1–17, https://doi.org/10.1016/j.semcancer.2017.05.011.
[69] W.H. Liao, M.Y. Hsiao, Y. Kung, A.P. Huang, W.S. Chen, Investigation of the therapeutic effect of doxorubicin combined with focused shockwave on glioblastoma, Front. Oncol. 11 (2021) 711088, https://doi.org/10.3389/fonc.2021.711088.
[70] X. Sun, et al., ImmunoPET imaging of c-Met using a nanobody-based tracer [(68)Ga]Ga-NOTA-PFCM01 in pancreatic ductal adenocarcinoma models and non-human primates, Eur. J. Nucl. Med. Mol. Imag. (2025), https://doi.org/10.1007/s00259-025-07441-6.
[71] E.A. Salvanou, et al., Lu-Labeled iron oxide nanoparticles functionalized with doxorubicin and bevacizumab as nanobrachytherapy agents against breast cancer, Molecules 29 (2024), https://doi.org/10.3390/molecules29051030, 177.
[72] M. Weller, et al., Targeted radionuclide therapy for gliomas: emerging clinical trial landscape, Neuro Oncol. 26 (2024) S208–s214, https://doi.org/10.1093/neuonc/noae125.
[73] D. Fischer, et al., The CAM Model-Q&A with experts, Cancers (Basel) 15 (2022), https://doi.org/10.3390/cancers15010191.
[74] D. Ribatti, The chick embryo chorioallantoic membrane as an experimental model to study in vivo angiogenesis in glioblastoma multiforme, Brain Res. Bull. 182 (2022) 26–29, https://doi.org/10.1016/j.brainresbull.2022.02.005.
[75] B. Schweiger, F.M. Kievit, Glioblastoma induced blood-brain barrier dysfunction via a paracrine mechanism that increases claudin-1 expression, Exp. Brain Res. 243 (2025) 70, https://doi.org/10.1007/s00221-025-07018-7.
[76] A.P. Ghosh, et al., Kinomic profiling identifies focal adhesion kinase 1 as a therapeutic target in advanced clear cell renal cell carcinoma, Oncotarget 8 (2017) 29220–29232, https://doi.org/10.18632/oncotarget.16352.
[77] A.N. Tran, et al., Increased sensitivity to radiochemotherapy in IDH1 mutant glioblastoma as demonstrated by serial quantitative MR volumetry, Neuro Oncol. 16 (2014) 414–420, https://doi.org/10.1093/neuonc/not198.
[78] R.J. Molenaar, J.P. Maciejewski, J.W. Wilmink, C.J.F. van Noorden, Wild-type and mutated IDH1/2 enzymes and therapy responses, Oncogene 37 (2018) 1949–1960, https://doi.org/10.1038/s41388-017-0077-z.
[79] T.K. Sears, C.M. Horbinski, K.D. Woolard, IDH1 mutant glioma is preferentially sensitive to the HDAC inhibitor panobinostat, J. Neuro Oncol. 154 (2021) 159–170, https://doi.org/10.1007/s11060-021-03829-0.